applied sciences

MDPI

Article

The Influence of Titanium Substitution on Phase Transition Energy and Crystalline Composition in the Complex $La_{2-x}Ti_xMo_2O_{9+x/2}$ System

Giedrė Gaidamavičienė [1], Jonas Labutis [1], Edgars Elsts [2], Jevgenijs Gabrusenoks [2], Marina Koņuhova [2,*], Anatoli I. Popov [2] and Artūras Žalga [1,*]

[1] Institute of Chemistry, Faculty of Chemistry and Geosciences, Vilnius University, Naugarduko Str. 24, 03225 Vilnius, Lithuania
[2] Institute of Solid State Physics, University of Latvia, 8 Kengaraga Str., LV-1063 Riga, Latvia
* Correspondence: marina.konuhova@cfi.lu.lv (M.K.); arturas.zalga@chf.vu.lt (A.Ž.)

Featured Application

This study presents the development of novel LAMOX-based, doped, complex multi-component $La_{2-x}Ti_xMo_2O_{9+x/2}$ systems, synthesized using innovative, environmentally friendly approaches. Investigating crystal structure evolution and thermal effects associated with phase transitions provides insight into the mechanisms governing ionic conductivity changes during high-temperature phase transitions. These findings establish a scientific basis for the potential application of such ceramic materials as solid electrolytes in solid oxide fuel cells, supporting their practical role in energy conversion technologies.

Abstract

The aqueous sol–gel preparation technique was successfully employed for synthesizing a homogeneous La–Ti–Mo–O tartrate gel precursor, and thermal treatment at 1000 °C promoted the formation of nanocrystalline complex $La_{2-x}Ti_xMo_2O_{9+x/2}$ ceramic. X-ray diffraction analysis revealed a consistent influence of increasing the degree of titanium substitution on the formation of the $La_2Mo_2O_3$ and La_2MoO_6 impurity phases within the crystalline mixture. Meanwhile, the stability of the high-temperature cubic β-$La_2Mo_2O_9$ phase in the $La_{2-x}Ti_xMo_2O_{9+x/2}$ system at room temperature highlighted the distinct influence of titanium content from structural and thermodynamic perspectives. However, the Raman spectroscopy analysis showed no distinct variations in the spectra of $La_{2-x}Ti_xMo_2O_{9+x/2}$ samples, suggesting a substantial effect of titanium on the phase transition behavior between the low-temperature monoclinic α-$La_2Mo_2O_9$ and the high-temperature cubic β-$La_2Mo_2O_9$ phases.

Keywords: sol–gel synthesis; phase transition; thermal analysis; X-ray diffraction; Rietveld refinement; Raman spectroscopy

Academic Editor: Marilou Cadatal Raduban

Received: 5 February 2026
Revised: 20 February 2026
Accepted: 21 February 2026
Published: 25 February 2026

1. Introduction

The potential applications of oxygen-ion-conducting solid electrolytes in the construction of galvanic cells for high-accuracy measurements of the thermodynamic and kinetic properties of oxygen-bearing systems, the development of oxygen sensors for both gas mixtures and liquid metals, and the investigation of high-temperature fuel cells have been known and explored for over 60 years [1–4]. However, their practical role in energy conversion has become particularly relevant only in recent years [5,6]. The increasing emphasis

on reducing the greenhouse effect, limiting fossil fuel combustion, and addressing the growing need for energy storage and consumption drives industrial advancements toward renewable and environmentally sustainable energy solutions across specialized sectors, such as aerospace and defense, and general consumer applications [6–11].

A possible solution to this problem directly relates to developing and advancing electrochemical systems for chemical-to-electrical energy conversion [12,13]. For this reason, there is a renewed focus on the classical solid oxide fuel cell (SOFC) concept, which is defined by the compatibility of porous electrodes with a dense oxygen-ion-conducting electrolyte layer [14,15].

Solid oxide fuel cells, consisting of a cathode, an anode, and an interposed electrolyte, operate as high-temperature energy conversion devices, transforming chemical energy into electrical energy [16]. In this process, oxygen undergoes reduction at the cathode. At the same time, oxide ions travel through the solid electrolyte toward the anode, facilitating the conversion of hydrogen gas into water molecules or hydrocarbons into water and carbon dioxide, inducing a controlled electron flow within the external circuit [17].

Thus, the cathode is typically a porous, oxidation-resistant electrochemical cell component [18,19]. In contrast, the negative electrode (anode) must resist reduction and be permeable to hydrogen or hydrocarbon gases [20]. Meanwhile, the solid electrolyte must possess a dense structure [21] to facilitate the directed transport of the required ions from one electrode to another while preventing electronic conductivity and gas permeation [22,23].

The compatibility of the solid electrolyte with the electrodes, enhanced oxygen ion conductivity, and negligible electronic conductivity are key factors determining the potentially beneficial device characteristics, which are primarily governed by the operating temperature [24]. The increased working temperature of the cell generally results in substantially higher fabrication and operating expenses while accelerating the degradation of the solid oxide fuel cell [25]. For example, conventional solid electrolytes, including yttria-stabilized zirconia (YSZ), demonstrate superior ionic conductivity in the temperature range of 800 °C to 1000 °C [26,27]. In contrast, gadolinium-doped ceria (GDC) operates at significantly lower temperatures, typically between 600 °C and 800 °C. However, under these conditions, it exhibits mixed ionic–electronic conductivity and increased sensitivity in a reducing environment [28]. The listed drawbacks of traditional electrolytes [29,30] create the need to explore alternative compounds or material systems whose composition, structure, ionic conductivity, and operating temperature meet modern industry's economic and environmental requirements.

From this perspective, a suitable candidate could be lanthanum molybdate ($La_2Mo_2O_9$), known under the acronym LAMOX, whose remarkable oxygen ion conductivity at elevated temperatures was first observed and published by Lacorre et al. in 2000 [31,32]. However, the main drawback of this complex oxide system lies in its reversible phase transition occurring between 500 °C and 600 °C, during which the low-temperature monoclinic α-$La_2Mo_2O_9$ phase [33] transforms into a high-temperature cubic polymorphic modification [34] with significantly enhanced oxygen ion conductivity [35]. The recrystallization processes occurring during this phase transition induce significant volume changes in the $La_2Mo_2O_9$ compound, which eventually deform and deteriorate the solid electrolyte's contact with the electrode surface [36,37]. Reducing the phase transition effect and stabilizing the cubic β-$La_2Mo_2O_9$ crystalline modification at room temperature remain key challenges in the practical application of this complex system.

For this reason, many contemporary scientific studies on the LAMOX system focus on modifying the $La_2Mo_2O_9$ crystalline phase by partially substituting lanthanum or molybdenum with other chemical elements [38–41]. The increasing compositional complexity of final multicomponent oxides, reflected in the greater number of constituent chemical

elements, narrows the spectrum of available synthesis methodologies. In this context, solid-state reaction technology dominates the scientific literature, as it theoretically enables the synthesis of final products with unrestricted compositions or doped with additives of diverse nature [21,42,43]. Nevertheless, the main drawback of this method is associated with the initial mixing stage of the starting components, which directly determines the final product's purity, homogeneity, and specific structural and morphological characteristics [44]. In order to avoid these undesirable side effects, the solid-state synthesis method is frequently modified during the mixing stage through the introduction of volatile and thermally labile additives, which improve the wetting of the precursor materials and promote more efficient homogenization [39]. This adverse effect may sometimes be counteracted by extending the heating period, implementing additional low-temperature annealing steps, or increasing the thermal energy driving the formation of the final oxide phase. In any case, the synthesis process becomes longer and more complex, consequently increasing the cost of obtaining the final product. Such circumstances create favorable conditions for searching for and applying alternative synthesis methods in complex system fabrication [45,46]. One of the viable alternatives is aqueous sol–gel technology, during which the initial reactants for final oxide formation are mixed at the molecular level in a selected solvent, forming a homogeneous gel that is subsequently applied as the precursor for dense ceramics and coatings with a wide range of thicknesses [47].

The economic efficiency, technological simplicity, and environmental friendliness associated with the application of the aqueous sol–gel method for the synthesis of single-phase $La_2Mo_2O_9$ solid electrolyte [48] motivated the objective of producing the complex $La_{2-x}Ti_xMo_2O_{9+x/2}$ system, in which lanthanum was partially substituted with titanium atoms for the first time. Furthermore, the additional novelty of this study is provided by the investigation of the thermal dynamics of the reversible α-$La_2Mo_2O_9 \leftrightarrow \beta$-$La_2Mo_2O_9$ equilibrium phase transition via differential thermal analysis, which, powered by X-ray diffraction results, indicated incorporation of Ti^{4+} ions into the $La_{2-x}Ti_xMo_2O_{9+x/2}$ complex oxide system.

2. Materials and Methods

This study describes the sequence of dissolution and complexation of individual metal ions in an aqueous medium using selected reagents. The qualitative characteristics of the reagents employed and the outcomes of their mutual interactions in an aqueous tartaric acid environment are also specified. The formation schemes of the resulting tartrate gels and the final ceramic materials, together with detailed descriptions of the preparation procedures, analytical techniques, and data analysis methods used for their characterization, are presented in the subsequent sections. The samples are designated according to their initial compositions, expressed as $La_{2-x}Ti_xMo_2O_{9+x/2}$.

2.1. Reagents and Materials

The complex oxide system with the initial composition $La_{2-x}Ti_xMo_2O_{9+x/2}$ was synthesized using high-purity reagents: MoO_3 (99.95%), La_2O_3 ($\geq$99.99%), and Ti (99.4%), all supplied by Alfa Aesar (Thermo Fisher Scientific, Haverhill, MA, USA). In this study, L(+)-tartaric acid ($C_4H_6O_6$, Carl Roth (Carl Roth GmbH + Co. KG, Karlsruhe, Germany), $\geq$99.5%), concentrated ammonia solution ($NH_3 \cdot H_2O$, Chempur (Chempur Feinchemikalien GmbH, Karlsruhe, Germany), 25%), and nitric acid (HNO_3, Eurochemicals (Eurochemicals UAB, Vilnius, Lithuania), 65%) were utilized for dissolving the initial reagents, forming complexes with the resulting salts, and adjusting the pH of the aqueous solution. The final product's physical, chemical, structural, and morphological properties are strongly influenced by the reagents and materials employed during the synthesis process. This is

particularly critical for preserving the appropriate molar ratios of the constituent elements within the resulting multicomponent oxide system. In this context, the purity of the starting reagents is of primary importance and may be significantly affected by environmental factors such as atmospheric composition, humidity, and temperature. Titanium and corresponding metal oxides are not the most convenient alternatives for aqueous sol–gel synthesis, but they meet the most cost-effective requirements for initial materials. Titanium exhibits the highest corrosion resistance among metallic elements, while molybdenum (VI) oxide is characterized by its significant inertness toward hydrolysis and oxidative environmental conditions. In contrast, lanthanum (III) oxide, due to its strong basicity, is more susceptible to reactions with atmospheric moisture and carbon dioxide. Consequently, before each synthesis procedure, La_2O_3 powder was subjected to additional heat treatment at 1000 °C to eliminate carbonate and hydroxide impurities.

2.2. Oxidative Dissolution and Complexation of Titanium Powders

The essential stage in the synthesis of the $La_{2-x}Ti_xMo_2O_{9+x/2}$ system is associated with the oxidation of metallic titanium powder in a concentrated aqueous hydrochloric acid solution [49], during which Ti^{3+} ions, coordinated by chloride ligands and complexed with tartaric acid, created favorable conditions for molecular-level mixing of the individual components and the generation of a homogeneous La–Ti–Mo–O tartrate gel. The titanium dissolution and complexation mechanism is schematically illustrated in Figure 1.

Titanium dissolution in concentrated hydrochloric acid:

$$2\,Ti\,(s) + 6\,HCl\,(aq) + 12\,H_2O\,(l) \rightarrow 2\,[Ti(OH_2)_6]Cl_3\,(aq) + 3\,H_2\,(g)$$

purplish-pink solution

Complexation reaction with a monodentate ligand (X):

$$[Ti(OH_2)_6]^{3+}\,(aq) + z\,X\,(aq) + n\,H_2O\,(l) \rightarrow [Ti\,(X)_z(OH_2)_{6-z-n}(OH)_n]^{3-n}\,(aq) + n\,H^+\,(aq)$$

Proposed complexation mechanism involving tartaric acid:

$$[Ti(OH_2)_6]Cl_3\,(aq) + 2\,H_2O\,(l) \rightarrow [Ti(OH_2)_4(OH)_2]Cl\,(aq) + 2\,HCl\,(aq)$$

$$[Ti(OH_2)_4(OH)_2]Cl\,(aq) + 2\,HOOC(CH(OH))_2COO^-\,(aq) \rightarrow [Ti(OH)_2(HOOC(CH(OH))_2COO)_2]^-\,(aq) + Cl^-\,(aq) + 4\,H_2O\,(l)$$

$$[Ti(OH)_2(HOOC(CH(OH))_2COO)_2]^-\,(aq) + HOOC(CH(OH))_2COOH\,(aq) \rightarrow [Ti(HOOC(CH(OH))_2COO)_3]^{2-}\,(aq) + 2\,H_2O\,(l)$$

Figure 1. Schematic diagram of the dissolution and complexation processes of metallic titanium in hydrochloric and tartaric acids.

It is noteworthy that during the dissolution of titanium in hydrochloric acid, the aqueous solution turns pink, which shifts to a light green upon mixing with the molybdate–tartrate aqueous mixture.

2.3. Synthesis Process and Methodology

The sol–gel method is a simple, cost-effective, and highly efficient technique for achieving a uniform distribution of atoms or ions, forming a homogeneous molecular-level mixture and facilitating the synthesis of single-phase ceramic materials. A schematic representation of this process is provided in Figure 2.

At the initial La–Ti–Mo–O tartrate gel synthesis stage, molybdenum (VI) oxide was dispersed in deionized water under continuous stirring and heating. To improve the solubility of MoO_3, a small amount of concentrated ammonia solution was added to the reaction mixture. The chemical reaction corresponding to the formation of ammonium molybdate in a basic solution is shown in Equation (1):

$$MoO_3\,(s) + 2\,NH_3{\cdot}H_2O\,(aq) \rightarrow (NH_4)_2MoO_4\,(aq) + H_2O\,(s) \quad (1)$$

Next, the ammonium molybdate is treated with tartaric acid, which acts as a ligand by forming complexes with MoO_4^{2-} ions and preventing the reversible precipitation of molybdenum (VI) oxide at lower pH values. This process is illustrated in Equation (2):

$$MoO_4^{2-}\ (aq) + 4\ C_4H_6O_6\ (aq) \leftrightarrow [(MoO_4)(C_4H_4O_6)_qH_r]^{(2+2q-r)-}\ (aq) + (2q - r)\ H^+\ (aq) + (4 - q)\ C_4H_6O_6\ (aq) \quad (2)$$

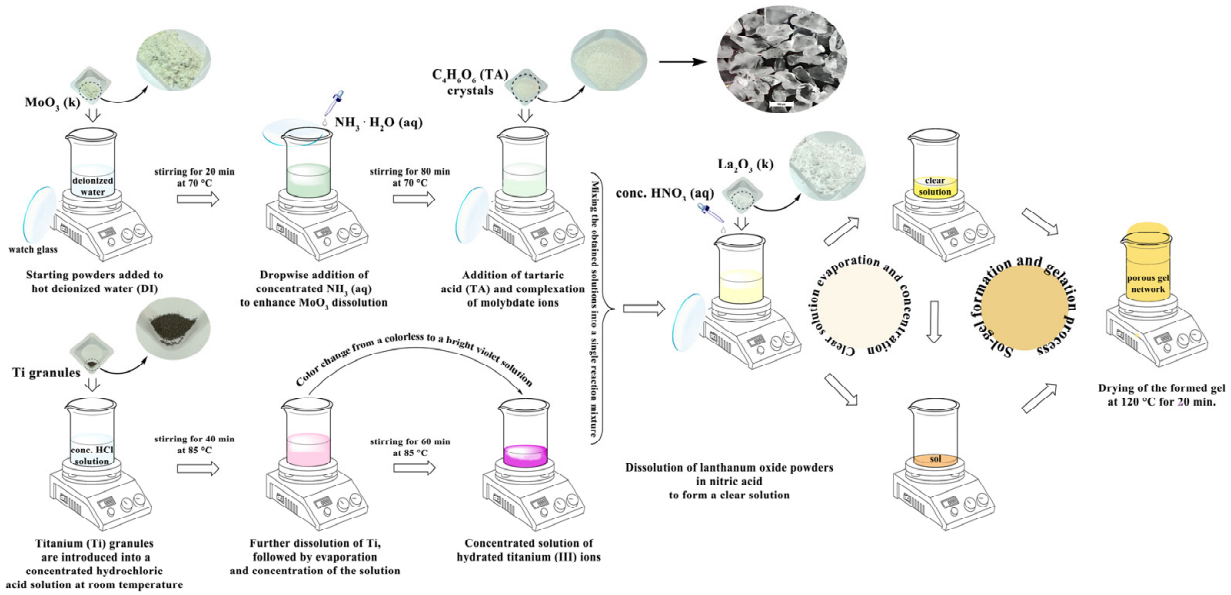

Figure 2. Synthesis scheme of the La–Ti–Mo–O tartrate precursor for $La_{2-x}Ti_xMo_2O_{9+x/2}$ ceramic.

In this case, an excess of tartaric acid was used (nMo/nTA = ¼ = 0.25), creating favorable conditions for the optimal complexation of molybdate ions. A similar complexation process of titanium ions (Figure 1) is evidenced by the colour change from light pink to pale yellow upon dissolving Ti powder in a concentrated aqueous hydrochloric acid solution and mixing it with tartaric acid. Next, the tartrate-based molybdate and titanium ion solutions were mixed, followed by the addition of lanthanum (III) oxide powder and concentrated nitric acid to the resulting clear, pale yellow solution. During this step, Ti^{3+} ions were oxidized to Ti^{4+} by nitric acid, after which the solution was subsequently concentrated. It is important to note that, during the final stage of solvent removal, a bright yellow viscous sol was formed, accompanied by the intense release of nitrogen oxide gases, and expanded into a light, yellow-brown homogeneous La–Ti–Mo–O tartrate gel precursor. The resulting porous structure formation was dried at 120 °C for 1 h and then ground for 20 min in an agate mortar to obtain a homogeneous fine powder. The homogeneity and amorphous nature of the fine La–Ti–Mo–O tartrate gel powder were confirmed by X-ray diffraction (XRD) analysis. The absence of residual chloride ions in the reaction mixture during gelation was confirmed by silver nitrate testing after re-dissolving the dried gel in water.

Finally, the La–Ti–Mo–O tartrate gel precursor powders synthesized via the aqueous sol–gel method were heat-treated at 1000 °C for 5 h in the air. The crystallinity of the resulting white ceramic material was examined by X-ray diffraction (XRD); phase transition characteristics were assessed by differential scanning calorimetry (DSC), and the vibrational modes of functional groups were analyzed using Raman spectroscopy.

2.4. Equipment, Instruments and Technical Specifications

The influence of titanium substitution on the enthalpy variations associated with phase transitions in the $La_{2-x}Ti_xMo_2O_{9+x/2}$ oxide system was quantitatively evaluated by differential scanning calorimetry (DSC) measurements performed on La–Ti–Mo–O

tartrate-derived ceramics heat-treated at 1000 °C. Thermal characterization was performed using a PerkinElmer STA 6000 simultaneous thermal analyzer (PerkinElmer, Waltham, MA, USA). Due to the technique's high sensitivity, approximately 20.3 mg of accurately weighed material was analyzed. The measurements were carried out under a dry-air atmosphere at a flow rate of 20 mL min^{-1} and ambient pressure, with a constant heating and cooling rate of 40 °C min^{-1}. Two consecutive thermal cycles were performed over the temperature range 300–800 °C. Instrumental background contributions were corrected by subtracting baseline signals obtained from empty alumina crucibles. The phase transition features were subsequently analyzed using Pyris 11 software, within the temperature ranges of 538.04–594.94 °C during heating and 594.94–496.71 °C during cooling.

The crystalline structure and phase assemblage of the obtained ceramic materials were examined by powder X-ray diffraction (XRD) coupled with Rietveld refinement. Data collection was carried out at ambient conditions using a Rigaku MiniFlex II diffractometer (Rigaku, Tokyo, Japan) operating with Cu Kα radiation (λ = 1.541838 Å). Diffraction patterns were acquired over a 2θ angular range of 5–80°, employing a step increment of 0.02° and a scanning speed of 10° min^{-1}. Prior to analysis, the powdered samples were uniformly distributed on a glass sample holder to enhance diffraction signal quality. Phase identification and quantitative evaluation were subsequently performed through Rietveld refinement using the X'Pert HighScore Plus software package (version 2.0a).

The Inorganic Crystal Structure Database (ICSD) and the Crystallography Open Database (COD) were employed for Rietveld refinement and the identification of crystalline phases. According to the COD, entry No. 1533393 [34] corresponds to a cubic $La_2Mo_2O_9$ phase crystallizing in the space group P213 (No. 198), while entry No. 4000583 [33] represents a monoclinic $La_2Mo_2O_9$ phase with the space group P1211 (No. 4). The ICSD entry No. 2634 [50] corresponds to monoclinic $La_2Mo_3O_{12}$, characterized by the space group C12/c1. Finally, ICSD entry No. 79807 [51] describes a tetragonal La_2MoO_6 phase crystallizing in the space group I41/acd.

This study primarily focuses on the phase composition and structural evolution of the $La_{2-x}Ti_xMo_2O_{9+x/2}$ system rather than on complete crystal structure determination. Therefore, comprehensive crystallographic parameters, including atomic coordinates, site occupancies, and thermal displacement factors, are not reported.

Local structural ordering and disorder effects induced by the substitution of lanthanum with titanium ions were investigated by Raman spectroscopy. Spectral measurements were performed using a TriVista 777 Raman system (Teledyne Princeton Instruments, Trenton, NJ, USA) equipped with a Peltier-cooled charge-coupled device (CCD) detector. Raman excitation was provided by a 785 nm diode laser, with the incident beam focused onto the sample surface. The scattered radiation was collected through an OLYMPUS BX53 optical microscope (Olympus, Tokyo, Japan).

3. Results and Discussion

This part of the work presents the results of differential scanning calorimetry (DSC), X-ray diffraction (XRD), and Raman spectroscopy for $La_{2-x}Ti_xMo_2O_{9+x/2}$ ceramics synthesized using the aqueous sol–gel method and heat-treated at 1000 °C. In addition, the DSC and XRD data generated and summarized in this work are based on measurements of the thermal effects of phase transitions and calculations for identifying the resulting crystalline phases, which are presented in a separate Appendix A.

3.1. Thermal Analysis

The high-temperature phase transition of the monoclinic double oxide to a cubic structure within the complex La–Mo–O system is characterized by an exothermic effect,

the thermal intensity of which directly depends on the $La_2Mo_2O_9$ concentration in the synthesized ceramic material. Thus, the numerical expression of the thermal effect determined during this structural change enables an accurate assessment of the amount of monoclinic $La_2Mo_2O_9$ double oxide in the synthesized ceramic. Considering that structural changes in the material can occur incompletely during the thermal process, two heating cycles of the ceramic were performed in this study, with the summarized results presented in Figure 3, respectively.

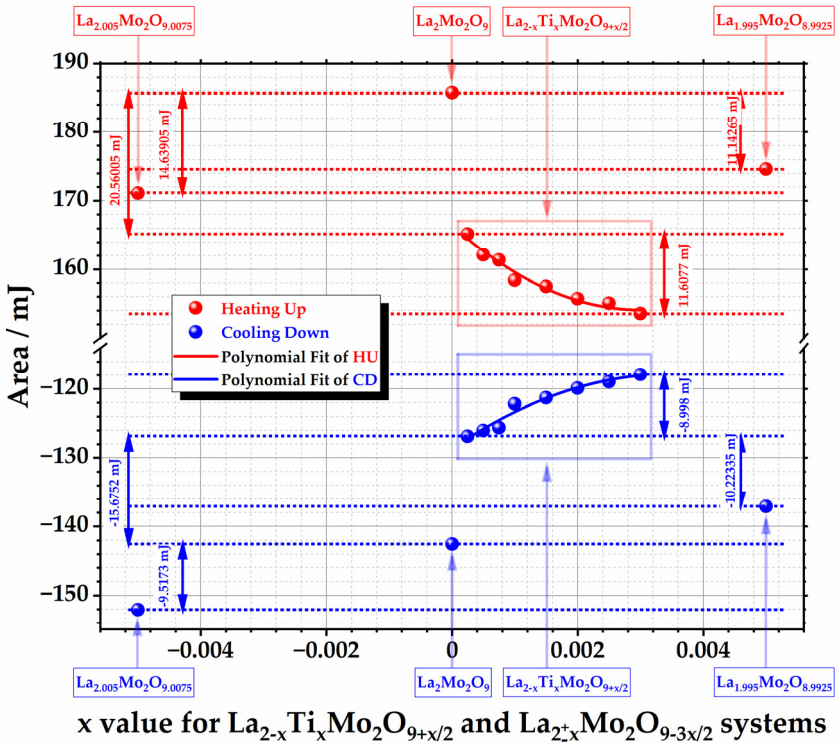

Figure 3. Dependence of phase transition heats on the initial molar composition in $La_{2\pm x}Mo_2O_{9\pm 3/2x}$ and $La_{2-x}Ti_xMo_2O_{9+x/2}$ complex systems.

The assessment of the thermal effects associated with phase transitions in complex $La_{2-x}Ti_xMo_2O_{9+x/2}$ oxide systems revealed that even a slight substitution of lanthanum with titanium ions leads to a relatively significant decrease in the heat flow change. In this case, the reduction of 20.56005 mJ in the heat associated with the phase transition is observed for $La_{1.99975}Ti_{0.00025}Mo_2O_{9.000125}$ (x = 0.00025) ceramic, compared to the double $La_{2.00}Mo_2O_{9.00}$ oxide system with an exothermic effect of 185.75205 mJ, indicating that even trace levels of Ti^{4+} substitution considerably influence the monoclinic-to-cubic transformation behavior. Increasing the Ti^{4+} substitution to x = 0.003 in $La_{2-x}Ti_xMo_2O_{9+x/2}$ further lowers the heat of phase transition by 11.6077 mJ, resulting in an exothermic effect of 153.5843 mJ for $La_{1.997}Ti_{0.003}Mo_2O_{9.0015}$. Although the decreasing enthalpy trend might suggest a direct correlation with the reduction in $La_{2.00}Mo_2O_{9.00}$-phase content in the ceramic, the sharp differences in the thermal effects observed for the non-stoichiometric $La_{1.995}Mo_2O_{8.9925}$ and $La_{2.005}Mo_2O_{9.0075}$ samples [52] indicate a more complex behavior. The thermal effect associated with the phase transition from monoclinic to cubic symmetry corresponds to 174.6094 mJ for $La_{1.995}Mo_2O_{8.9925}$ and 171.113 mJ for $La_{2.005}Mo_2O_{9.0075}$. In contrast, titanium-substituted compositions such as $La_{1.99975}Ti_{0.00025}Mo_2O_{9.000125}$ and $La_{1.997}Ti_{0.003}Mo_2O_{9.0015}$ exhibit reduced enthalpy values of 165.192 mJ and 153.5843 mJ, respectively. These results support an important conclusion regarding the enhanced influence of titanium ions on the phase transition energetics in the complex $La_{2-x}Ti_xMo_2O_{9+x/2}$ oxide system.

The results of the DSC analysis presented in this section indicate that the considerable decrease in phase transition heat flow observed in the $La_{2-x}Ti_xMo_2O_{9+x/2}$ system is predominantly attributed to the impact of Ti^{4+} ion incorporation on the formation of the $La_2Mo_2O_9$ crystal lattice.

3.2. X-Ray Diffraction

X-ray diffraction (XRD) analysis was employed to support DSC data interpretation. The Appendix B includes full diffraction patterns and refinement calculations, with Figure 4 summarizing phase composition in $La_{2\pm x}Mo_2O_{9\pm3/2x}$ and $La_{2-x}Ti_xMo_2O_{9+x/2}$ ceramic systems.

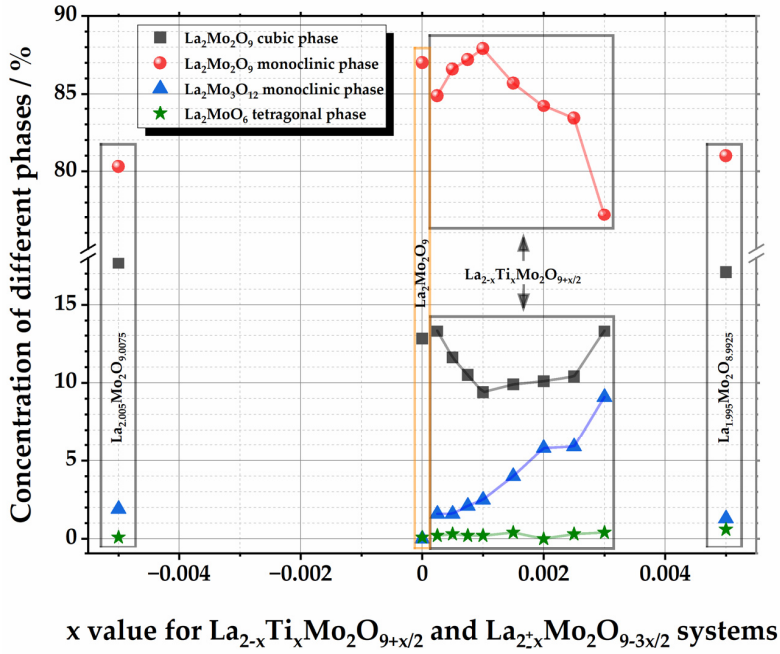

Figure 4. Concentration dependence of different crystalline phases on the initial molar composition in $La_{2\pm x}Mo_2O_{9\pm3/2x}$ and $La_{2-x}Ti_xMo_2O_{9+x/2}$ complex oxide systems.

It is important to note that even a very slight substitution of lanthanum with titanium ions results in a relatively significant formation of the secondary $La_2Mo_3O_{12}$ phase in the resulting crystalline mixture, with its concentration increasing sharply beyond the substitution level of $La_{1.999}Ti_{0.001}Mo_2O_{9.0005}$ (x = 0.001). The increase in the amount of impurity compounds in the crystalline mixture is directly related to changes in the monoclinic/cubic phase ratio of the $La_2Mo_2O_9$ oxide system. In this case, a slight tendency for an increase in the $La_2Mo_3O_{12}$ impurity phase is observed as the substitution level of lanthanum with titanium ions reaches x = 0.001. Meanwhile, the concentration of the monoclinic phase increases and exceeds its amount in the undoped $La_2Mo_2O_9$ oxide. Further deviation from stoichiometry in the oxide system significantly increases $La_2Mo_3O_{12}$ content, reaching nearly 10% at the highest Ti^{4+} substitution level (x = 0.001). The observed effect of the impurity phase is closely related to the stabilization of the high-temperature cubic modification at room temperature in the $La_2Mo_2O_9$ complex oxide system, as demonstrated by the significant decline in monoclinic phase concentration to as low as 77% at a substitution level of x = 0.003. These results indicate that the increase in the amount of lanthanum molybdate impurity phases in the crystalline mixture of the $La_2Mo_2O_9$ complex system promotes the stabilization of the high-temperature cubic phase at room temperature. In this case, the influence of titanium ions on the composition of crystalline phases is significantly greater than that of either lanthanum excess or deficiency in the final ceramic mixture.

Based on the information presented in this section, the titanium substitution effect in the $La_{2-x}Ti_xMo_2O_{9+x/2}$ system can be identified as the principal factor responsible for the formation of the monoclinic $La_2Mo_3O_{12}$ secondary phase and the room-temperature stabilization of the high-temperature cubic $La_2Mo_2O_9$ phase.

It should be noted that, due to the low titanium concentration and the detection limits of the available XRD instrumentation, no direct evidence of titanium-containing phases was observed in the diffraction patterns. The presence of titanium in the samples is inferred from the initial composition $La_{2-x}Ti_xMo_2O_{9+x/2}$ and the synthesis procedure.

3.3. Raman Spectroscopy

Raman spectroscopy is vital for examining local ordering and disorder within the crystal lattice. The spectra obtained from the crystalline state display lattice modes—vibrations caused by translational and rotational motions of molecules in the crystalline lattice [53]. In this work, the Raman spectroscopical investigation was performed for the $La_{1.99}Mo_2O_{8.985}$, $La_{2.00}Mo_2O_{9.00}$, $La_{2-x}Ti_xMo_2O_{9+x/2}$ and $La_{2.01}Mo_2O_{9.015}$ samples to confirm the formation of MoO_4 tetrahedra in the monoclinic $La_2Mo_2O_9$ crystal lattice and the effect of impurity phases on the specific vibrations of Mo–O bonds. The corresponding results are presented in Figures 5 and 6. Furthermore, Table 1 details the vibrational mode frequencies and their associated symmetries of the MoO_4^{2-} ion. [54].

Table 1. Measured vibrational frequencies of Raman peaks (cm^{-1}) and their assignments for $La_{1.99}Mo_2O_{8.985}$, $La_{2.00}Mo_2O_{9.00}$, $La_{2-x}Ti_xMo_2O_{9+x/2}$, and $La_{2.01}Mo_2O_{9.015}$ samples at room temperature [1].

Internal Mode of Free Ions	Raman Frequency/cm^{-1}	Assignment
ν_1 of MoO_4^{2-}	965–815 vs	Symmetric stretching
ν_3 of MoO_4^{2-}	750 m	Asymmetric stretching
ν_2 of MoO_4^{2-}	370–300 sh	Symmetric bending
ν_4 of MoO_4^{2-}	370–300 sh	Asymmetric bending
–	450–540 w	MoO_5^{4-} or MoO_6^{6-}

[1] Relative intensities: vs: very strong; m: medium; w: weak; sh: shoulder.

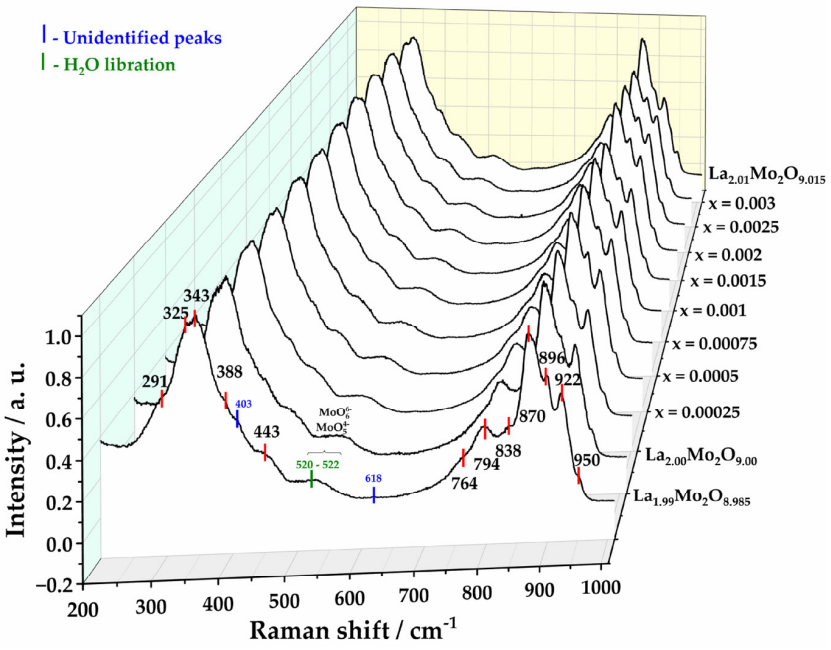

Figure 5. Raman spectra of the $La_{1.99}Mo_2O_{8.985}$, $La_{2.00}Mo_2O_{9.00}$, $La_{2-x}Ti_xMo_2O_{9+x/2}$, and $La_{2.01}Mo_2O_{9.015}$ samples.

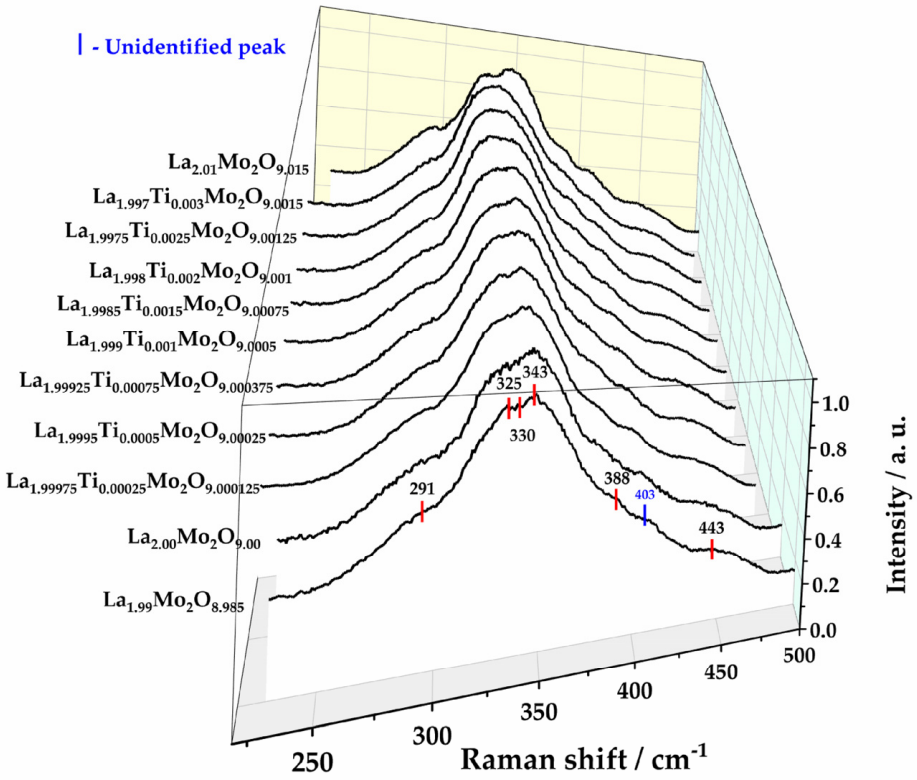

Figure 6. Raman spectra of lanthanum molybdates with different initial molar compositions in the 250 cm^{-1}–500 cm^{-1} spectral range.

According to the selection rules, the monoclinic unit cell of the $La_2Mo_2O_9$ compound is expected to exhibit 51 Raman-active modes (25 Ag + 26 Bg) [55]. However, the number of experimentally observed peaks is significantly lower than the predicted value for the monoclinic symmetry. This notable reduction in Raman-active modes (Figure 5) is commonly observed in nanometric polycrystalline materials with large and complex unit cells [56]. The bending and stretching vibrational modes of molybdate tetrahedra (MoO_4^{2-}) in aqueous salt solutions and crystalline phases exhibit strong similarities, leading to Raman peaks located in comparable spectral regions.

Figure 5 presents the Raman spectra of $La_{1.99}Mo_2O_{8.985}$, $La_{2.00}Mo_2O_{9.00}$, $La_{2-x}Ti_xMo_2O_{9+x/2}$, and $La_{2.01}Mo_2O_{9.015}$ compounds, which reveal nearly identical positions and intensities of the characteristic vibrational bands. These results provide additional evidence supporting earlier conclusions on the crystalline composition and structural homogeneity of the synthesized materials. In this context, the observed Raman bands appear to be determined by the distribution and orientation of molybdate functional units within the crystal lattice of the $La_2Mo_2O_9$ double oxide phase.

On the other hand, within the more pronounced spectral interval of 300–400 cm^{-1} (Figure 6), variations in the intensity distribution of Raman-active modes are evident, particularly for samples with initial molar compositions $La_{1.99}Mo_2O_{8.985}$ and $La_{2.01}Mo_2O_{9.015}$. For the $La_{1.99}Mo_2O_{8.985}$ and $La_{2.00}Mo_2O_{9.00}$ compounds, the intensity ratio of the internal symmetric bending (ν_2 of MoO_4^{2-}) and asymmetric bending (ν_4 of MoO_4^{2-}) modes at 325 cm^{-1} and 343 cm^{-1}, respectively, remains comparable. By contrast, Ti-substituted samples exhibit a merging of these modes, which can be ascribed to an increasing fraction of the impurity monoclinic $La_2Mo_3O_{12}$ crystalline phase in the resulting ceramic material.

In conclusion, Raman analysis of lanthanum molybdate ceramics demonstrates that an increased content of the impurity $La_2Mo_3O_{12}$ phase primarily affects the intensities of the ν_2 (symmetric bending) and ν_4 (asymmetric bending) internal modes of MoO_4^{2-}

groups. The corresponding change in their intensity ratio is most pronounced in the Raman spectrum of the sample for $La_{1.997}Ti_{0.003}Mo_2O_{9.0015}$ composition.

4. Conclusions

The phase-transition enthalpy values of titanium-substituted lanthanum molybdate $La_{2-x}Ti_xMo_2O_{9+x/2}$ ceramics synthesized by the aqueous sol–gel method and heat-treated at 1000 °C differed significantly from the corresponding thermal characteristics of single-phase $La_{2.00}Mo_2O_{9.00}$ and nonstoichiometric $La_{1.99}Mo_2O_{8.985}$ and $La_{2.01}Mo_2O_{9.015}$ compositions. X-ray diffraction analysis showed that both titanium substitution and initial nonstoichiometry increased the content of secondary phases in the synthesized ceramics. It was found that the introduction of titanium into the multicomponent $La_{2-x}Ti_xMo_2O_{9+x/2}$ system affects the phase evolution and thermal behavior of the synthesized ceramics primarily by forming secondary crystalline phases. In particular, the presence of titanium promotes the formation of the $La_2Mo_3O_{12}$ impurity phase, which leads to a reduction in the energy of the high-temperature phase transition. The concentration of this secondary phase was shown to directly affect the vibrational modes of the molybdate groups, as evidenced by Raman spectroscopy. Based on the obtained structural, phase-composition, and spectroscopic results, it can be concluded that titanium ions do not significantly substitute lanthanum within the $La_2Mo_2O_9$ crystal lattice.

Author Contributions: Conceptualization, A.I.P. and A.Ž.; methodology, G.G., J.L., E.E., J.G. and A.Ž.; software, E.E., J.G. and A.Ž.; validation, E.E., J.G. and A.Ž.; formal analysis, A.Ž.; investigation, G.G., J.L. and A.Ž.; resources, G.G., J.L. and A.Ž.; data curation, A.Ž.; writing—original draft preparation, A.I.P., M.K. and A.Ž.; writing—review and editing, A.I.P. and A.Ž.; visualization, E.E., A.Ž.; supervision, A.I.P. and A.Ž.; project administration, M.K., A.I.P.; funding acquisition, A.I.P. All authors have read and agreed to the published version of the manuscript.

Funding: This work was supported by LZP projects Nr. OSI_PIP_BioPhoT-2025/2-0069 (Anatolijs Popovs).

Institutional Review Board Statement: Not applicable.

Informed Consent Statement: Not applicable.

Data Availability Statement: The original contributions presented in this study are included in the article. Further inquiries can be directed to the corresponding author.

Acknowledgments: The authors would like to express their sincere appreciation to all those who contributed to the advancement of this research. The manuscript was reviewed and edited by the authors, who assume full responsibility for the content of this publication.

Conflicts of Interest: The authors declare no conflicts of interest.

Abbreviations

The following abbreviations are used in this manuscript:

DSC	differential scanning calorimetry
GDC	gadolinium-doped ceria
LAMOX	lanthanum molybdate ($La_2Mo_2O_9$)
TA	tartaric acid
YSZ	yttria-stabilized zirconia

Appendix A. The DSC Curves and Phase Transition Thermoanalytical Data of the Corresponding $La_{2-x}Ti_xMo_2O_{9+x/2}$ Ceramic, as the Source for the Data Analyzed in Section 3.1

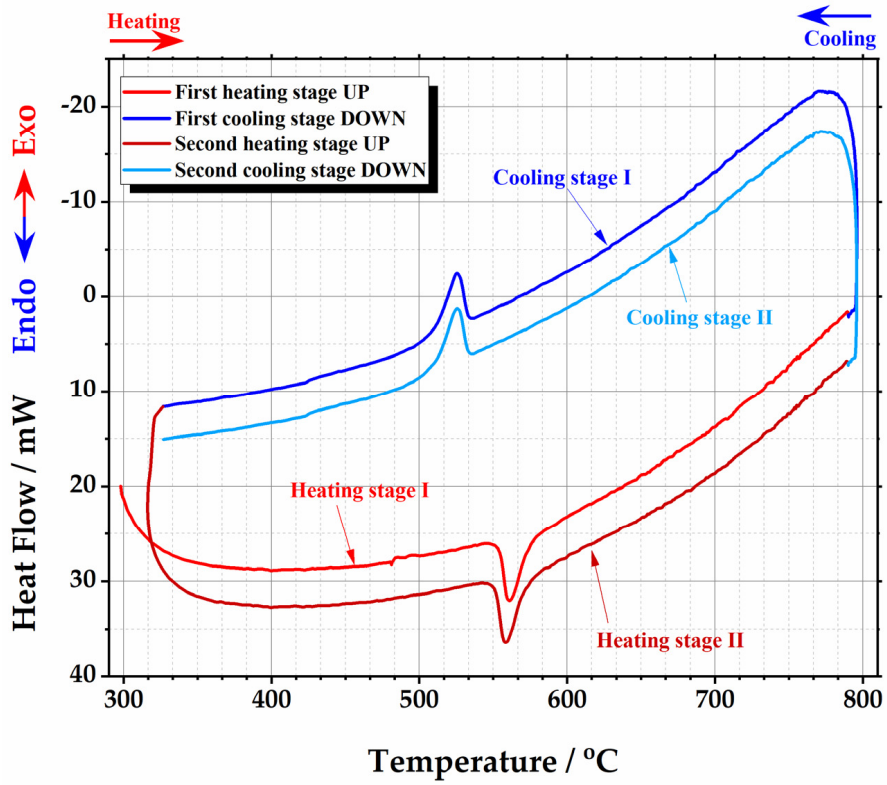

Figure A1. DSC curve of the phase transition cycles for $La_{1.99975}Ti_{0.00025}Mo_2O_{9.000125}$ ceramic heat-treated at 1000 °C.

Table A1. Thermoanalytical data of the phase transition for $La_{1.99975}Ti_{0.00025}Mo_2O_{9.000125}$ ceramic composition.

Stage Up I Range of Temperature from 538.04 °C to 594.94 °C				
Onset/°C	End/°C	Area/mJ	ΔH/J/g	Peak/°C
553.94	575.23	160.002	7.8588	561.09
Stage up II Range of temperature from 538.04 °C to 594.94 °C				
Onset/°C	End/°C	Area/mJ	ΔH/J/g	Peak/°C
551.13	573.16	170.382	8.3686	558.69
Average of the phase transition stages up				
Onset/°C	End/°C	Area/mJ	ΔH/J/g	Peak/°C
552.535	574.195	165.192	8.1137	559.89
Stage down I Range of temperature from 553.61 °C to 496.71 °C				
Onset/°C	End/°C	Area/mJ	ΔH/J/g	Peak/°C
532.82	511.63	−126.157	−6.1964	525.39
Stage down II Range of temperature from 553.61 °C to 496.71 °C				
Onset/°C	End/°C	Area/mJ	ΔH/J/g	Peak/°C
532.79	511.09	−127.575	−6.2661	525.61
Average of the phase transition stages down				
Onset/°C	End/°C	Area/mJ	ΔH/J/g	Peak/°C
532.805	511.36	−126.866	−6.23125	525.50

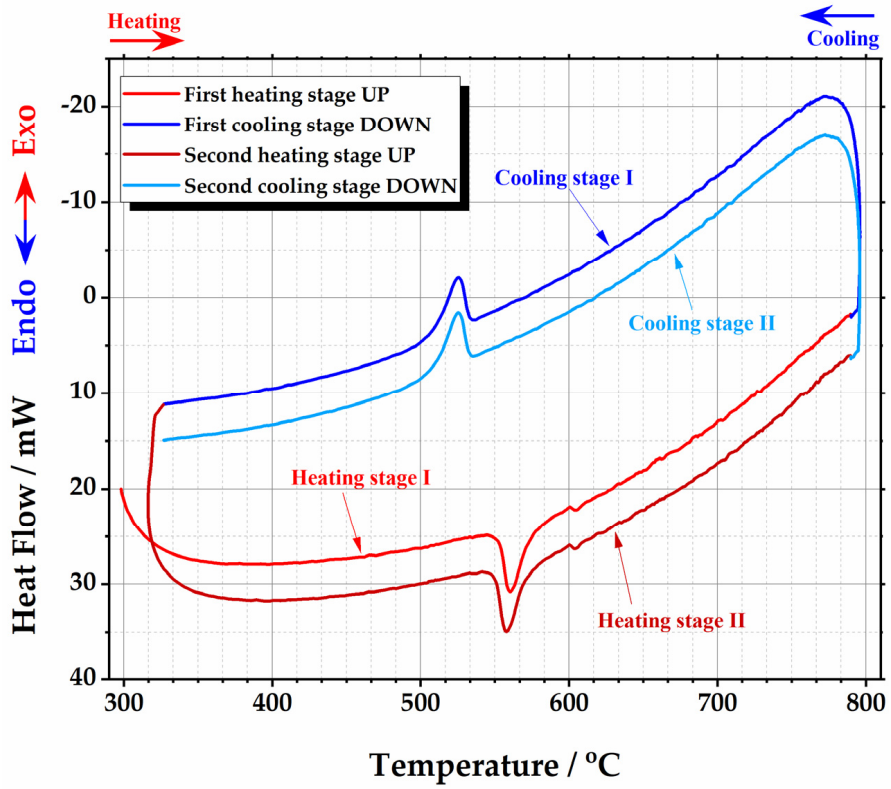

Figure A2. DSC curve of the phase transition cycles for $La_{1.9995}Ti_{0.0005}Mo_2O_{9.00025}$ ceramic heat-treated at 1000 °C.

Table A2. Thermoanalytical data of the phase transition for $La_{1.9995}Ti_{0.0005}Mo_2O_{9.00025}$ ceramic composition.

Stage Up I Range of Temperature from 538.04 °C to 594.94 °C				
Onset/°C	End/°C	Area/mJ	ΔH/J/g	Peak/°C
553.00	574.20	160.952	7.9056	560.31
Stage up II Range of temperature from 538.04 °C to 594.94 °C				
Onset/°C	End/°C	Area/mJ	ΔH/J/g	Peak/°C
550.13	571.81	163.269	8.0194	558.20
Average of the phase transition stages up				
Onset/°C	End/°C	Area/mJ	ΔH/J/g	Peak/°C
551.565	573.005	162.1105	7.9625	559.255
Stage down I Range of temperature from 553.61 °C to 496.71 °C				
Onset/°C	End/°C	Area/mJ	ΔH/J/g	Peak/°C
532.83	509.82	−126.015	−6.1896	524.85
Stage down II Range of temperature from 553.61 °C to 496.71 °C				
Onset/°C	End/°C	Area/mJ	ΔH/J/g	Peak/°C
532.56	511.01	−126.01	−6.1893	525.25
Average of the phase transition stages down				
Onset/°C	End/°C	Area/mJ	ΔH/J/g	Peak/°C
532.695	510.415	−126.0125	−6.18945	525.05

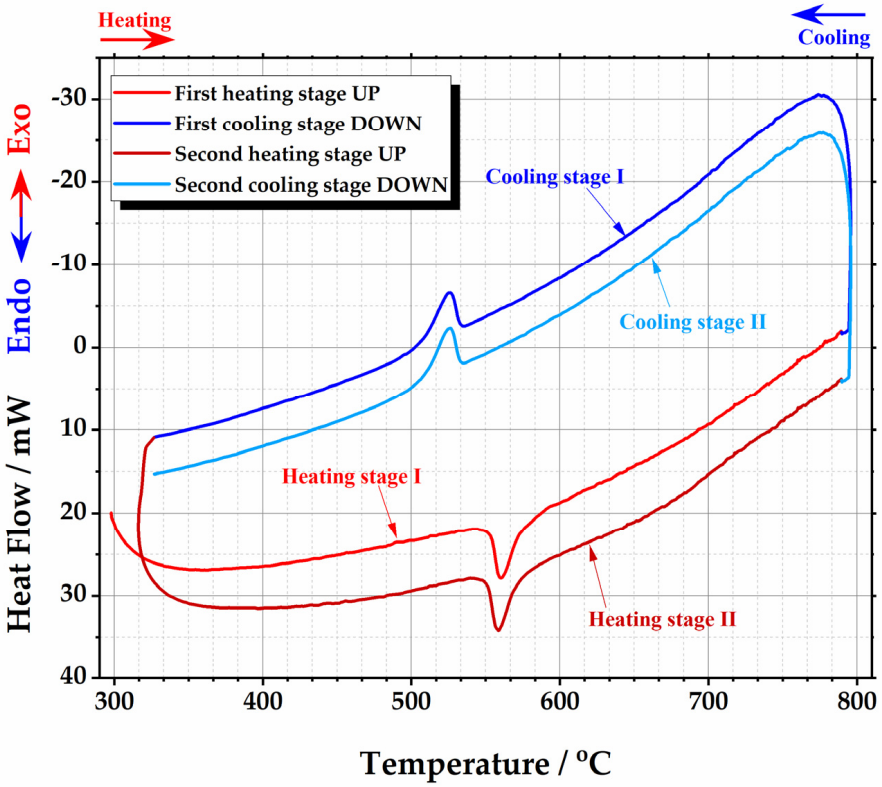

Figure A3. DSC curve of the phase transition cycles for $La_{1.99925}Ti_{0.00075}Mo_2O_{9.000375}$ ceramic heat-treated at 1000 °C.

Table A3. Thermoanalytical data of the phase transition for $La_{1.99925}Ti_{0.00075}Mo_2O_{9.000375}$ ceramic composition.

Stage Up I Range of Temperature from 538.04 °C to 594.94 °C				
Onset/°C	End/°C	Area/mJ	ΔH/J/g	Peak/°C
553.14	575.11	161.618	7.9306	560.38
Stage up II Range of temperature from 538.04 °C to 594.94 °C				
Onset/°C	End/°C	Area/mJ	ΔH/J/g	Peak/°C
550.92	572.25	161.129	7.9066	558.65
Average of the phase transition stages up				
Onset/°C	End/°C	Area/mJ	ΔH/J/g	Peak/°C
552.03	573.68	161.3735	7.9186	559.515
Stage down I Range of temperature from 553.61 °C to 496.71 °C				
Onset/°C	End/°C	Area/mJ	ΔH/J/g	Peak/°C
532.75	508.41	−125.651	−6.1657	524.94
Stage down II Range of temperature from 553.61 °C to 496.71 °C				
Onset/°C	End/°C	Area/mJ	ΔH/J/g	Peak/°C
532.65	508.58	−125.574	−6.1619	524.97
Average of the phase transition stages down				
Onset/°C	End/°C	Area/mJ	ΔH/J/g	Peak/°C
532.70	508.495	−125.6125	−6.1638	524.955

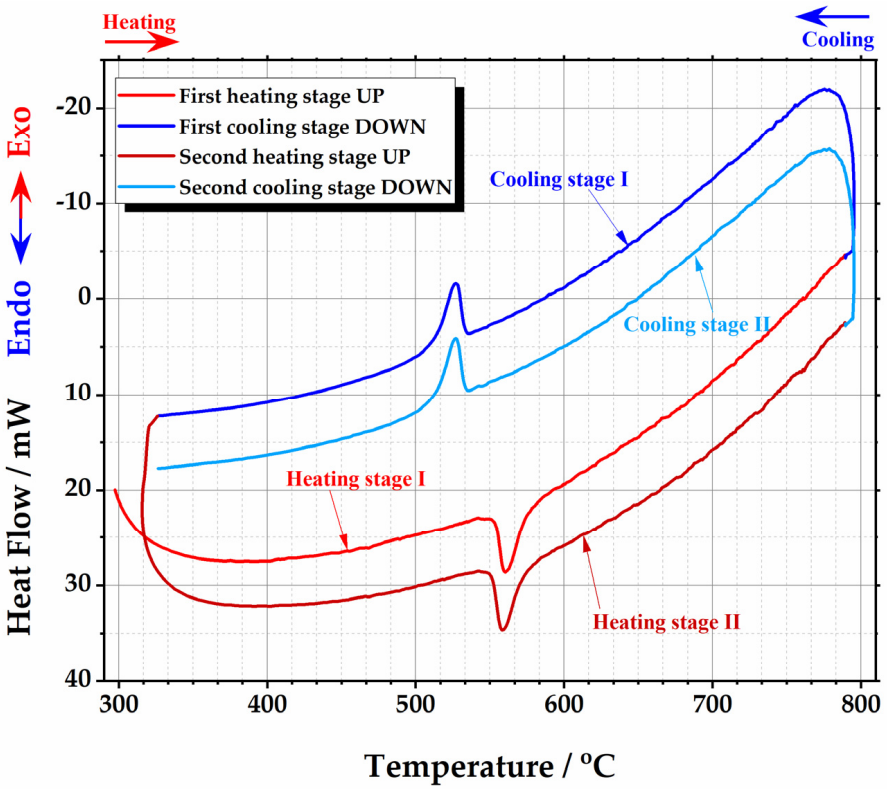

Figure A4. DSC curve of the phase transition cycles for $La_{1.999}Ti_{0.001}Mo_2O_{9.0005}$ ceramic heat-treated at 1000 °C.

Table A4. Thermoanalytical data of the phase transition for $La_{1.999}Ti_{0.001}Mo_2O_{9.0005}$ ceramic composition.

Stage Up I Range of Temperature from 538.04 °C to 594.94 °C				
Onset/°C	End/°C	Area/mJ	ΔH/J/g	Peak/°C
553.47	576.00	158.128	7.7578	560.37
Stage up II Range of temperature from 538.04 °C to 594.94 °C				
Onset/°C	End/°C	Area/mJ	ΔH/J/g	Peak/°C
551.39	573.44	158.691	7.7854	559.06
Average of the phase transition stages up				
Onset/°C	End/°C	Area/mJ	ΔH/J/g	Peak/°C
552.43	574.72	158.4095	7.7716	559.715
Stage down I Range of temperature from 553.61 °C to 496.71 °C				
Onset/°C	End/°C	Area/mJ	ΔH/J/g	Peak/°C
533.14	513.83	−122.2	−5.9952	526.93
Stage down II Range of temperature from 553.61 °C to 496.71 °C				
Onset/°C	End/°C	Area/mJ	ΔH/J/g	Peak/°C
532.95	513.88	−122.152	−5.9928	526.56
Average of the phase transition stages down				
Onset/°C	End/°C	Area/mJ	ΔH/J/g	Peak/°C
533.045	513.855	−122.176	−5.994	526.745

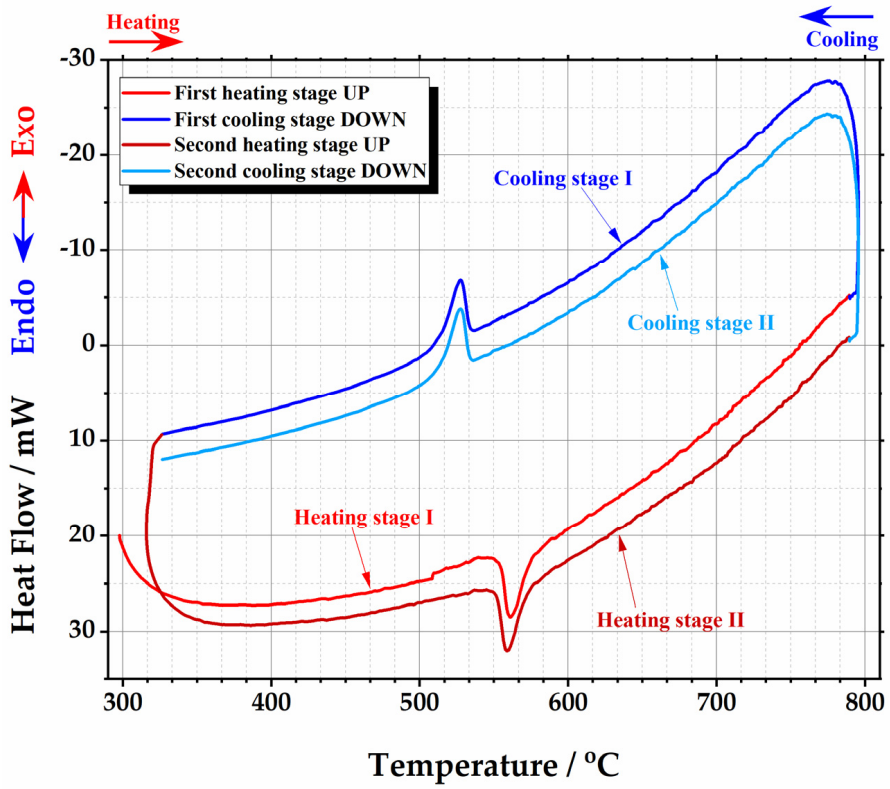

Figure A5. DSC curve of the phase transition cycles for $La_{1.9985}Ti_{0.0015}Mo_2O_{9.00075}$ ceramic heat-treated at 1000 °C.

Table A5. Thermoanalytical data of the phase transition for $La_{1.9985}Ti_{0.0015}Mo_2O_{9.00075}$ ceramic composition.

Stage Up I Range of Temperature from 538.04 °C to 594.94 °C				
Onset/°C	End/°C	Area/mJ	ΔH/J/g	Peak/°C
554.67	574.21	156.874	7.7031	561.44
Stage up II Range of temperature from 538.04 °C to 594.94 °C				
Onset/°C	End/°C	Area/mJ	ΔH/J/g	Peak/°C
551.88	571.85	158.129	7.7647	559.16
Average of the phase transition stages up				
Onset/°C	End/°C	Area/mJ	ΔH/J/g	Peak/°C
553.275	573.03	157.5015	7.7339	560.30
Stage down I Range of temperature from 553.61 °C to 496.71 °C				
Onset/°C	End/°C	Area/mJ	ΔH/J/g	Peak/°C
533.77	514.30	−120.868	−5.9351	527.26
Stage down II Range of temperature from 553.61 °C to 496.71 °C				
Onset/°C	End/°C	Area/mJ	ΔH/J/g	Peak/°C
533.44	514.06	−121.682	−5.9751	527.39
Average of the phase transition stages down				
Onset/°C	End/°C	Area/mJ	ΔH/J/g	Peak/°C
533.605	514.18	−121.275	−5.9551	527.325

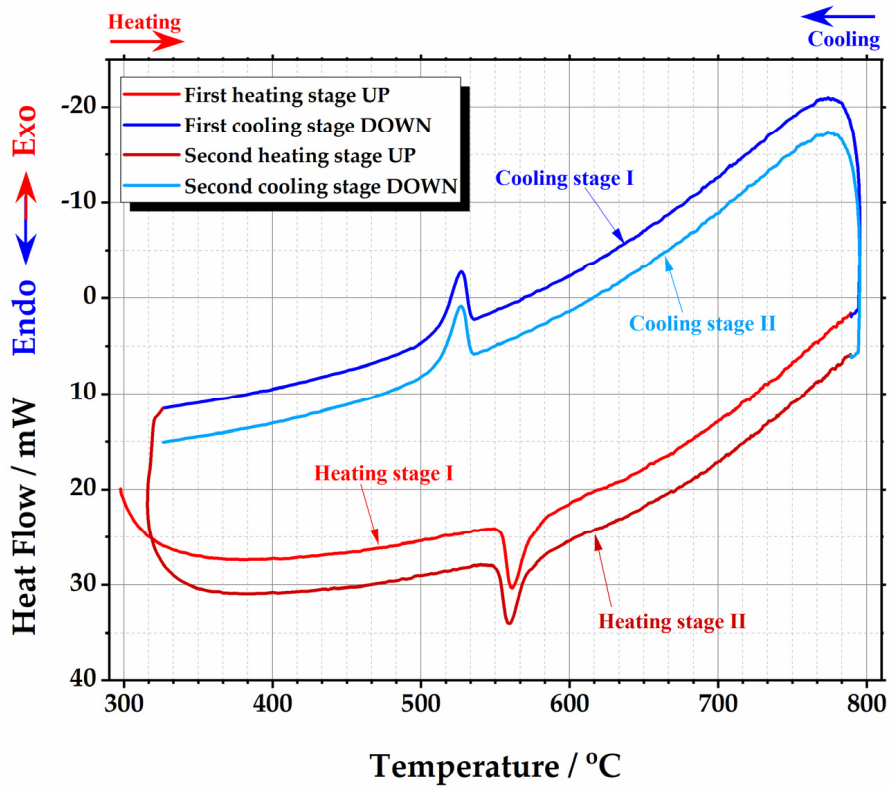

Figure A6. DSC curve of the phase transition cycles for $La_{1.998}Ti_{0.002}Mo_2O_{9.001}$ ceramic heat-treated at 1000 °C.

Table A6. Thermoanalytical data of the phase transition for $La_{1.998}Ti_{0.002}Mo_2O_{9.001}$ ceramic composition.

Stage Up I Range of Temperature from 538.04 °C to 594.94 °C				
Onset/°C	End/°C	Area/mJ	ΔH/J/g	Peak/°C
554.34	574.42	154.831	7.6007	561.49
Stage up II Range of temperature from 538.04 °C to 594.94 °C				
Onset/°C	End/°C	Area/mJ	ΔH/J/g	Peak/°C
551.82	572.92	156.545	7.6848	559.80
Average of the phase transition stages up				
Onset/°C	End/°C	Area/mJ	ΔH/J/g	Peak/°C
553.08	573.67	155.688	7.64275	560.645
Stage down I Range of temperature from 553.61 °C to 496.71 °C				
Onset/°C	End/°C	Area/mJ	ΔH/J/g	Peak/°C
533.39	512.68	−120.177	−5.8995	526.97
Stage down II Range of temperature from 553.61 °C to 496.71 °C				
Onset/°C	End/°C	Area/mJ	ΔH/J/g	Peak/°C
533.30	513.54	−119.58	−5.8702	526.91
Average of the phase transition stages down				
Onset/°C	End/°C	Area/mJ	ΔH/J/g	Peak/°C
533.345	513.11	−119.8785	−5.88485	526.94

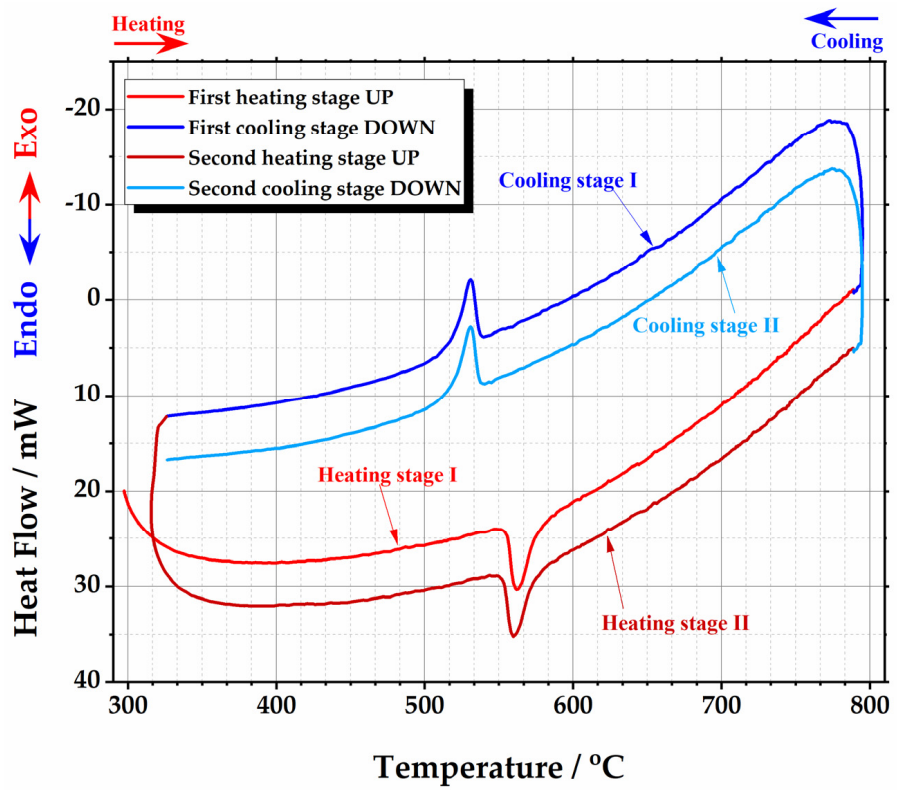

Figure A7. DSC curve of the phase transition cycles for $La_{1.9975}Ti_{0.0025}Mo_2O_{9.00125}$ ceramic heat-treated at 1000 °C.

Table A7. Thermoanalytical data of the phase transition for $La_{1.9975}Ti_{0.0025}Mo_2O_{9.00125}$ ceramic composition.

Stage Up I Range of Temperature from 538.04 °C to 594.94 °C				
Onset/°C	End/°C	Area/mJ	ΔH/J/g	Peak/°C
555.36	576.17	154.22	7.5711	562.72
Stage up II Range of temperature from 538.04 °C to 594.94 °C				
Onset/°C	End/°C	Area/mJ	ΔH/J/g	Peak/°C
553.17	573.53	155.939	7.6555	559.80
Average of the phase transition stages up				
Onset/°C	End/°C	Area/mJ	ΔH/J/g	Peak/°C
554.265	574.85	155.0795	7.6133	561.26
Stage down I Range of temperature from 553.61 °C to 496.71 °C				
Onset/°C	End/°C	Area/mJ	ΔH/J/g	Peak/°C
536.88	520.49	−119.106	−5.8473	530.77
Stage down II Range of temperature from 553.61 °C to 496.71 °C				
Onset/°C	End/°C	Area/mJ	ΔH/J/g	Peak/°C
536.75	519.79	−118.803	−5.8324	530.75
Average of the phase transition stages down				
Onset/°C	End/°C	Area/mJ	ΔH/J/g	Peak/°C
536.815	520.14	−118.9545	−5.83985	530.76

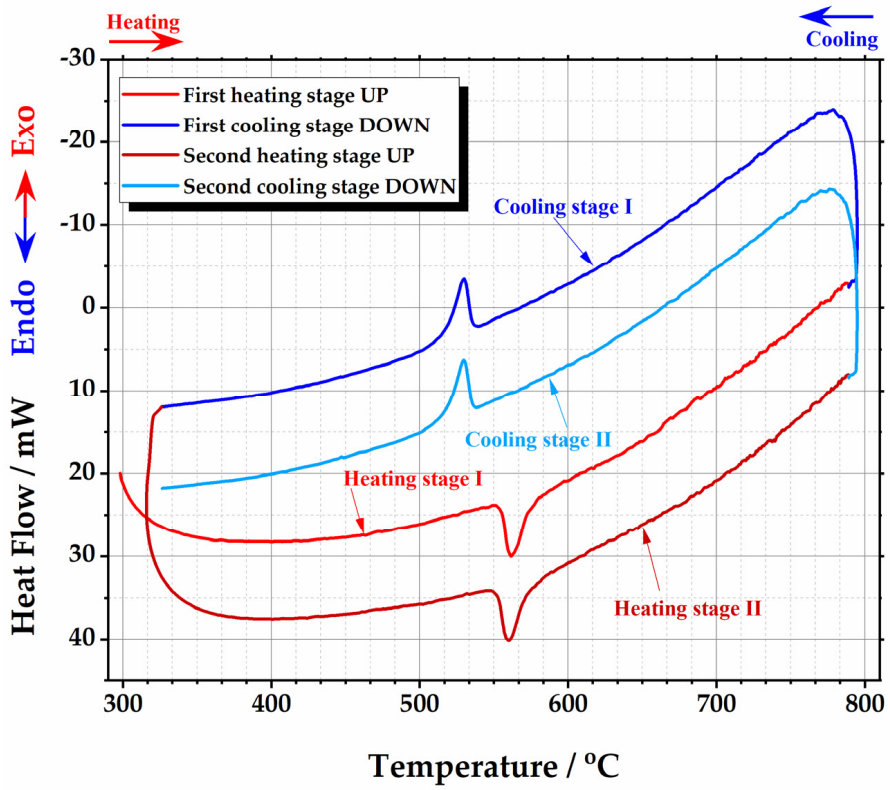

Figure A8. DSC curve of the phase transition cycles for $La_{1.997}Ti_{0.003}Mo_2O_{9.0015}$ ceramic heat-treated at 1000 °C.

Table A8. Thermoanalytical data of the phase transition for $La_{1.997}Ti_{0.003}Mo_2O_{9.0015}$ ceramic composition.

Stage Up I Range of Temperature from 538.04 °C to 594.94 °C				
Onset/°C	End/°C	Area/mJ	ΔH/J/g	Peak/°C
555.22	575.01	153.9787	7.5474	561.68
Stage up II Range of temperature from 538.04 °C to 594.94 °C				
Onset/°C	End/°C	Area/mJ	ΔH/J/g	Peak/°C
552.45	572.74	153.1899	7.5087	560.36
Average of the phase transition stages up				
Onset/°C	End/°C	Area/mJ	ΔH/J/g	Peak/°C
553.835	573.875	153.5843	7.52805	561.02
Stage down I Range of temperature from 553.61 °C to 496.71 °C				
Onset/°C	End/°C	Area/mJ	ΔH/J/g	Peak/°C
535.45	519.65	−118.2000	−5.7937	529.95
Stage down II Range of temperature from 553.61 °C to 496.71 °C				
Onset/°C	End/°C	Area/mJ	ΔH/J/g	Peak/°C
535.32	518.94	−117.5360	−5.7611	529.78
Average of the phase transition stages down				
Onset/°C	End/°C	Area/mJ	ΔH/J/g	Peak/°C
535.385	519.295	−117.8680	−5.7774	529.865

Appendix B. The X-Ray Diffraction Patterns and Rietveld Refinement Results for the Ceramic Samples, Which Serve as the Source of the Data Analyzed in Section 3.2

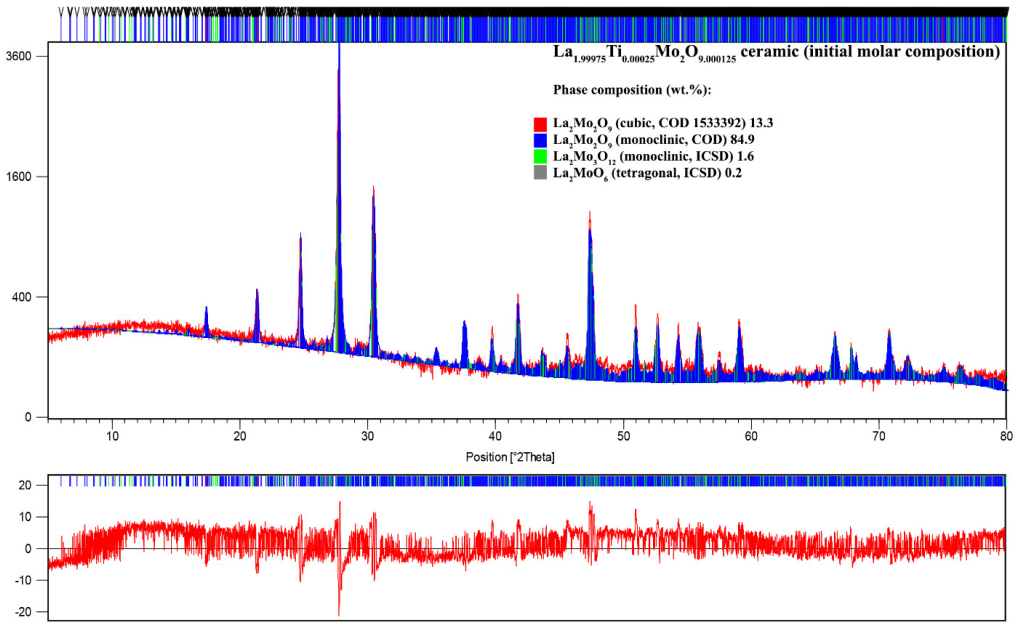

Figure A9. XRD pattern pressed by Rietveld refinement for the $La_{1.99975}Ti_{0.00025}Mo_2O_{9.000125}$ ceramic composition.

Table A9. Crystal system, mass fraction, crystallite size, and lattice parameters for the $La_{1.99975}Ti_{0.00025}Mo_2O_{9.000125}$ ceramic heat-treated at 1000 °C.

Initial Ceramic Composition	Crystal System/Molar Composition	Mass Fraction/%	Crystallite Size/nm	Unit Cell					
				Parameter			Angle		
				a/Å	b, Å	c, Å	α/°	β/°	γ/°
$La_{1.99975}Ti_{0.00025}Mo_2O_{9.000125}$	Cubic/$La_2Mo_2O_9$	13.3	43.09	7.14774	7.14774	7.14774	90.00000	90.00000	90.00000
	Monoclinic/$La_2Mo_2O_9$	84.9	86.67	14.29685	21.42117	28.50959	90.00000	90.41711	90.00000
	Monoclinic/$La_2Mo_3O_{12}$	1.6	39.55	17.13356	11.91913	16.13515	90.00000	108.48440	90.00000
	Tetragonal/La_2MoO_6	0.2	30.13	5.74433	5.74433	33.95038	90.00000	90.00000	90.00000

Table A10. Crystal system, mass fraction, crystallite size, and lattice parameters for the $La_{1.9995}Ti_{0.0005}Mo_2O_{9.00025}$ ceramic heat-treated at 1000 °C.

Initial Ceramic Composition	Crystal System/Molar Composition	Mass Fraction/%	Crystallite Size/nm	Unit Cell					
				Parameter			Angle		
				a/Å	b, Å	c, Å	α/°	β/°	γ/°
$La_{1.9995}Ti_{0.0005}Mo_2O_{9.00025}$	Cubic/$La_2Mo_2O_9$	11.6	48.47	7.14732	7.14732	7.14732	90.00000	90.00000	90.00000
	Monoclinic/$La_2Mo_2O_9$	86.6	101.43	14.29474	21.42595	28.52505	90.00000	90.42402	90.00000
	Monoclinic/$La_2Mo_3O_{12}$	1.6	64.72	17.10397	11.93450	16.10056	90.00000	108.63430	90.00000
	Tetragonal/La_2MoO_6	0.3	34.32	5.87002	5.87002	31.53833	90.00000	90.00000	90.00000

Table A11. Crystal system, mass fraction, crystallite size, and lattice parameters for the $La_{1.99925}Ti_{0.00075}Mo_2O_{9.000375}$ ceramic heat-treated at 1000 °C.

Initial Ceramic Composition	Crystal System/Molar Composition	Mass Fraction/%	Crystallite Size/nm	Unit Cell					
				Parameter			Angle		
				a/Å	b, Å	c, Å	α/°	β/°	γ/°
$La_{1.99925}Ti_{0.00075}Mo_2O_{9.000375}$	Cubic/$La_2Mo_2O_9$	10.5	41.77	7.15176	7.15176	7.15176	90.00000	90.00000	90.00000
	Monoclinic/$La_2Mo_2O_9$	87.2	65.42	14.30060	21.43204	28.52604	90.00000	90.42526	90.00000
	Monoclinic/$La_2Mo_3O_{12}$	2.1	44.31	17.11233	11.93314	16.09865	90.00000	108.54920	90.00000
	Tetragonal/La_2MoO_6	0.2	28.51	5.81296	5.81296	31.72586	90.00000	90.00000	90.00000

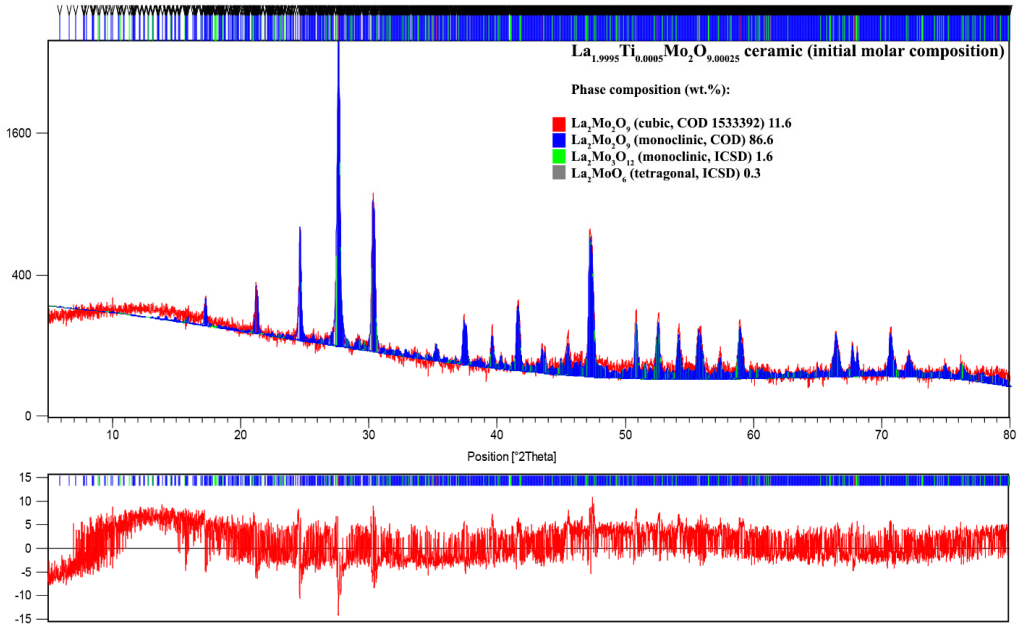

Figure A10. XRD pattern processed by Rietveld refinement for the $La_{1.9995}Ti_{0.0005}Mo_2O_{9.00025}$ ceramic composition.

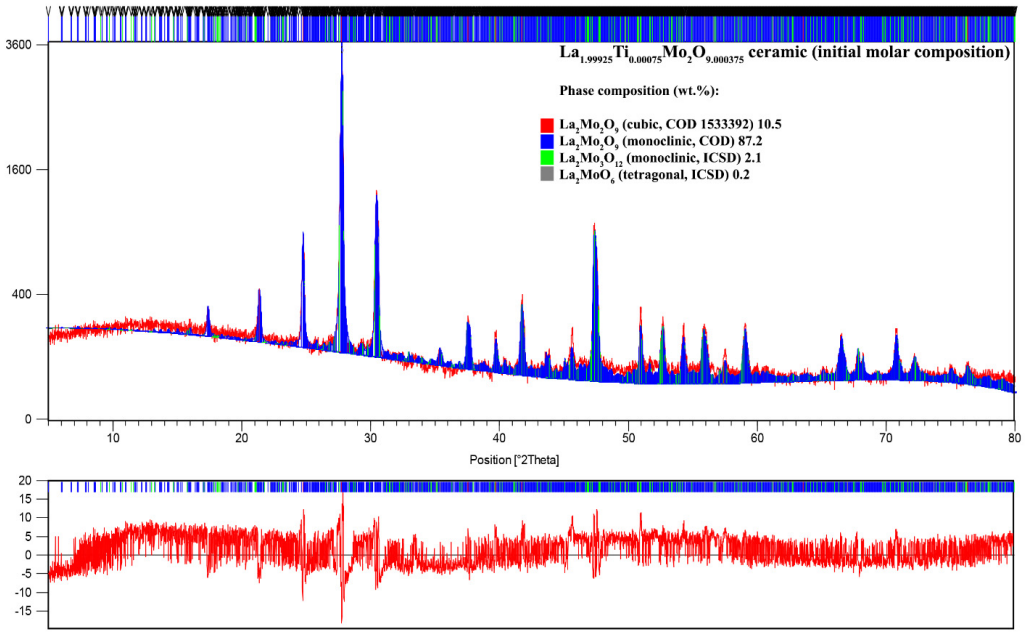

Figure A11. XRD pattern processed by Rietveld refinement for the $La_{1.99925}Ti_{0.00075}Mo_2O_{9.000375}$ ceramic composition.

Table A12. Crystal system, mass fraction, crystallite size, and lattice parameters for the $La_{1.999}Ti_{0.001}Mo_2O_{9.0005}$ ceramic heat-treated at 1000 °C.

Initial Ceramic Composition	Crystal System/Molar Composition	Mass Fraction/%	Crystallite Size/nm	Unit Cell					
				Parameter			Angle		
				a/Å	b, Å	c, Å	α/°	β/°	γ/°
$La_{1.999}Ti_{0.001}Mo_2O_{9.0005}$	Cubic/$La_2Mo_2O_9$	9.4	45.42	7.15177	7.15177	7.15177	90.00000	90.00000	90.00000
	Monoclinic/$La_2Mo_2O_9$	87.9	83.97	14.30054	21.43590	28.53332	90.00000	90.42794	90.00000
	Monoclinic/$La_2Mo_3O_{12}$	2.5	49.00	17.14078	11.92556	16.01975	90.00000	108.88280	90.00000
	Tetragonal/La_2MoO_6	0.2	29.40	5.79111	5.79111	31.69264	90.00000	90.00000	90.00000

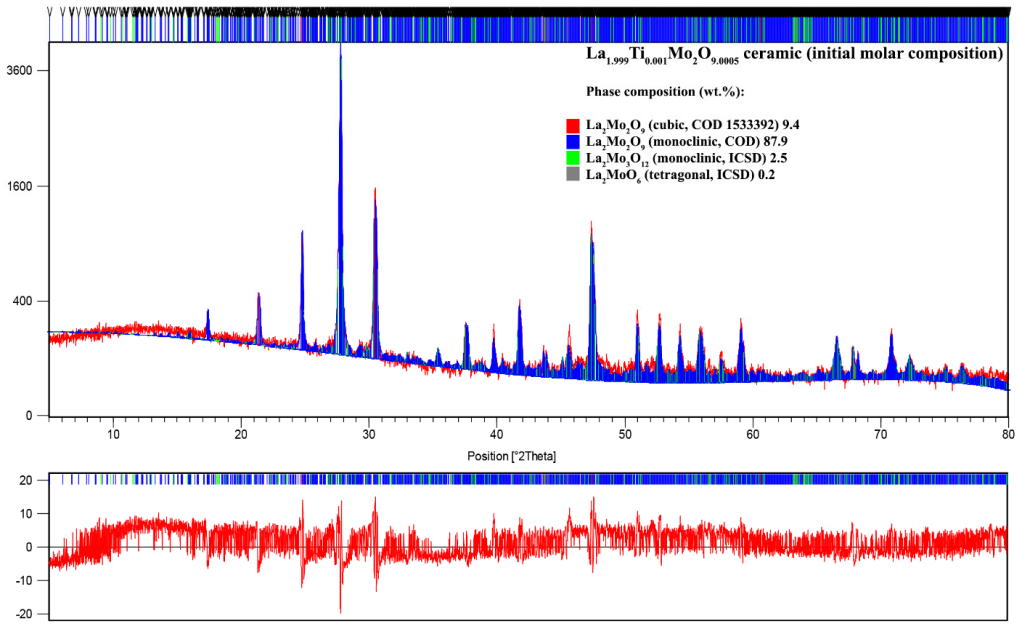

Figure A12. XRD pattern processed by Rietveld refinement for the $La_{1.999}Ti_{0.001}Mo_2O_{9.0005}$ ceramic composition.

Table A13. Crystal system, mass fraction, crystallite size, and lattice parameters for the $La_{1.9985}Ti_{0.0015}Mo_2O_{9.00075}$ ceramic heat-treated at 1000 °C.

Initial Ceramic Composition	Crystal System/Molar Composition	Mass Fraction/%	Crystallite Size/nm	Unit Cell					
				Parameter			Angle		
				a/Å	b, Å	c, Å	α/°	β/°	γ/°
$La_{1.9985}Ti_{0.0015}Mo_2O_{9.00075}$	Cubic/$La_2Mo_2O_9$	9.9	43.11	7.15154	7.15154	7.15154	90.00000	90.00000	90.00000
	Monoclinic/$La_2Mo_2O_9$	85.7	77.13	14.29876	21.42490	28.52146	90.00000	90.43916	90.00000
	Monoclinic/$La_2Mo_3O_{12}$	4.0	31.89	17.11449	11.87091	16.04972	90.00000	109.02870	90.00000
	Tetragonal/La_2MoO_6	0.4	28.59	5.85697	5.85697	31.96749	90.00000	90.00000	90.00000

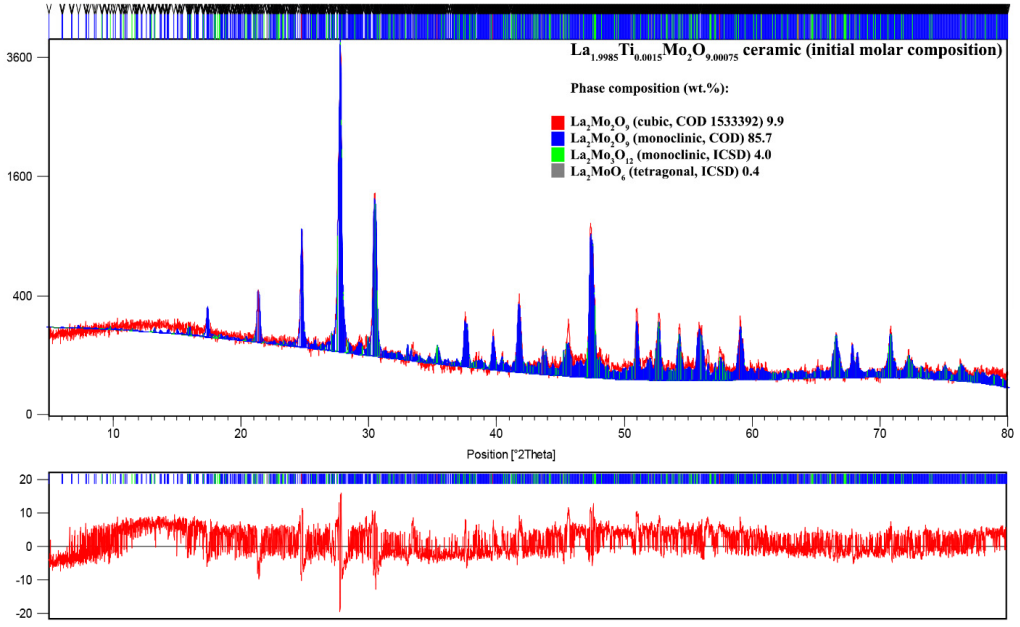

Figure A13. XRD pattern processed by Rietveld refinement for the $La_{1.9985}Ti_{0.0015}Mo_2O_{9.00075}$ ceramic composition.

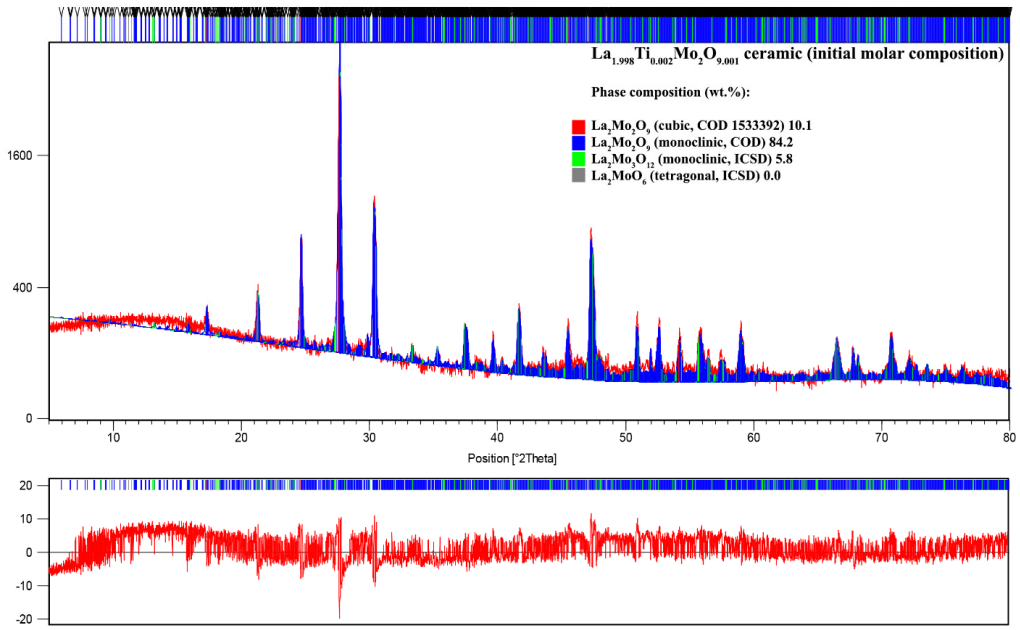

Figure A14. XRD pattern processed by Rietveld refinement for the $La_{1.998}Ti_{0.002}Mo_2O_{9.001}$ ceramic composition.

Table A14. Crystal system, mass fraction, crystallite size, and lattice parameters for the $La_{1.998}Ti_{0.002}Mo_2O_{9.001}$ ceramic heat-treated at 1000 °C.

Initial Ceramic Composition	Crystal System/Molar Composition	Mass Fraction/%	Crystallite Size/nm	Unit Cell					
				Parameter			Angle		
				a/Å	b, Å	c, Å	α/°	β/°	γ/°
$La_{1.998}Ti_{0.002}Mo_2O_{9.001}$	Cubic/$La_2Mo_2O_9$	10.1	44.94	7.14819	7.14819	7.14819	90.00000	90.00000	90.00000
	Monoclinic/$La_2Mo_2O_9$	84.2	84.55	14.29327	21.42161	28.51472	90.00000	90.43036	90.00000
	Monoclinic/$La_2Mo_3O_{12}$	5.8	39.46	16.89953	11.86142	15.97722	90.00000	108.49770	90.00000
	Tetragonal/La_2MoO_6	0.0	–	–	–	–	–	–	–

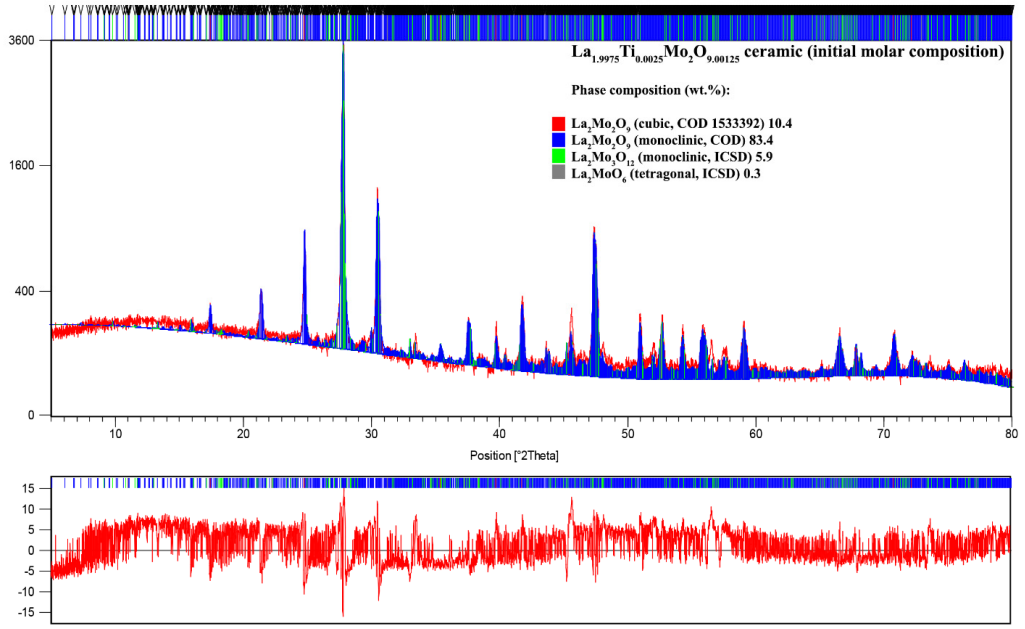

Figure A15. XRD pattern processed by Rietveld refinement for the $La_{1.9975}Ti_{0.0025}Mo_2O_{9.00125}$ ceramic composition.

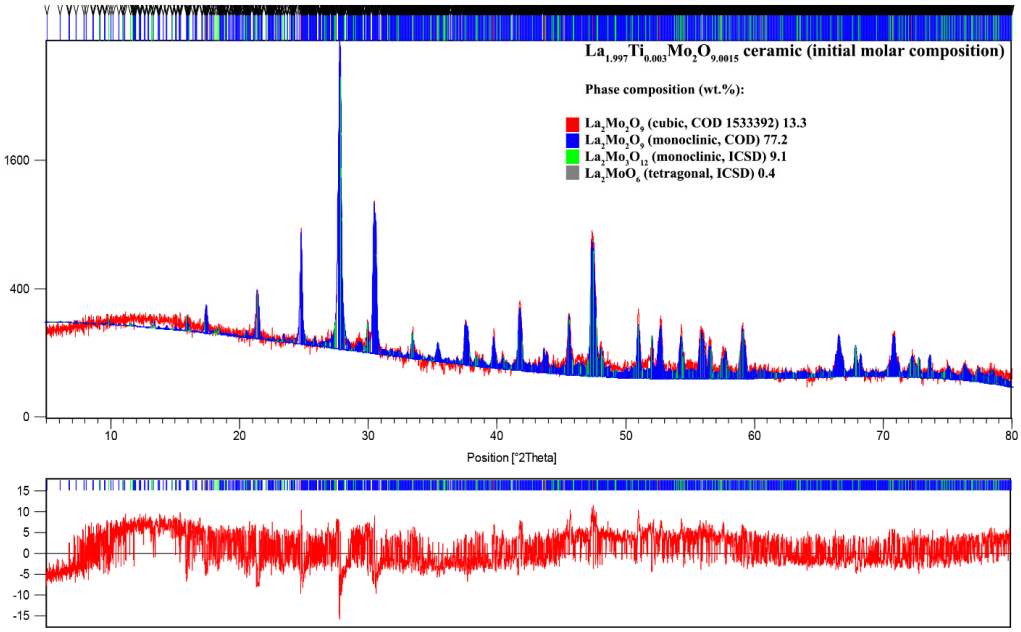

Figure A16. XRD pattern processed by Rietveld refinement for the $La_{1.997}Ti_{0.003}Mo_2O_{9.0015}$ ceramic composition.

Table A15. Crystal system, mass fraction, crystallite size, and lattice parameters for the $La_{1.9975}Ti_{0.0025}Mo_2O_{9.00125}$ ceramic heat-treated at 1000 °C.

Initial Ceramic Composition	Crystal System/Molar Composition	Mass Fraction/%	Crystallite Size/nm	Unit Cell					
				Parameter			Angle		
				a/Å	b, Å	c, Å	α/°	β/°	γ/°
$La_{1.9975}Ti_{0.0025}Mo_2O_{9.00125}$	Cubic/$La_2Mo_2O_9$	10.4	42.20	7.15750	7.15750	7.15750	90.00000	90.00000	90.00000
	Monoclinic/$La_2Mo_2O_9$	83.4	69.58	14.30539	21.43762	28.53926	90.00000	90.43098	90.00000
	Monoclinic/$La_2Mo_3O_{12}$	5.9	36.88	17.13456	11.86412	16.02840	90.00000	108.86070	90.00000
	Tetragonal/La_2MoO_6	0.3	27.62	5.79986	5.79986	31.83075	90.00000	90.00000	90.00000

Table A16. Crystal system, mass fraction, crystallite size, and lattice parameters for the $La_{1.997}Ti_{0.003}Mo_2O_{9.0015}$ ceramic heat-treated at 1000 °C.

Initial Ceramic Composition	Crystal System/Molar Composition	Mass Fraction/%	Crystallite Size/nm	Unit Cell					
				Parameter			Angle		
				a/Å	b, Å	c, Å	α/°	β/°	γ/°
$La_{1.997}Ti_{0.003}Mo_2O_{9.0015}$	Cubic/$La_2Mo_2O_9$	13.3	46.02	7.15220	7.15220	7.15220	90.00000	90.00000	90.00000
	Monoclinic/$La_2Mo_2O_9$	77.2	91.23	14.29833	21.42930	28.53137	90.00000	90.43802	90.00000
	Monoclinic/$La_2Mo_3O_{12}$	9.1	42.99	16.89683	11.87091	15.98331	90.00000	108.47970	90.00000
	Tetragonal/La_2MoO_6	0.4	32.33	5.83955	5.83955	32.01361	90.00000	90.00000	90.00000

References

1. Etsell, T.H.; Flengas, S.N. Electrical properties of solid oxide electrolytes. *Chem. Rev.* **1970**, *70*, 339–376. [CrossRef]
2. Subbarao, E.C.; Maiti, H.S. Solid electrolytes with oxygen ion conduction. *Solid State Ion.* **1984**, *11*, 317–338. [CrossRef]
3. Badwal, S.P.S.; Ciacchi, F.T. Oxygen-ion conducting electrolyte materials for solid oxide fuel cells. *Ionics* **2000**, *6*, 1–21. [CrossRef]
4. Li, J.; Cai, Q.; Horri, B.A. Highly conductive and stable electrolytes for solid oxide electrolysis and fuel cells: Fabrication, characterisation, recent progress and challenges. *Mater. Adv.* **2025**, *6*, 39–83. [CrossRef]
5. Ye, T.; Li, L.; Zhang, Y. Recent progress in solid electrolytes for energy storage devices. *Adv. Funct. Mater.* **2020**, *30*, 2000077. [CrossRef]
6. Vinchhi, P.; Khandla, M.; Chaudhary, K.; Pati, R. Recent advances on electrolyte materials for SOFC: A review. *Inorg. Chem. Commun.* **2023**, *152*, 110724. [CrossRef]
7. Maiti, T.K.; Majhi, J.; Maiti, S.K.; Singh, J.; Dixit, P.; Rohilla, T.; Ghosh, S.; Bhushan, S.; Chattopadhyay, S. Zirconia-and ceria-based electrolytes for fuel cell applications: Critical advancements toward sustainable and clean energy production. *Environ. Sci. Pollut. Res.* **2022**, *29*, 64489–64512. [CrossRef]

8. Stambouli, A.B.; Traversa, E. Solid oxide fuel cells (SOFCs): A review of an environmentally clean and efficient source of energy. *Renew. Sustain. Energy Rev.* **2002**, *6*, 433–455. [CrossRef]
9. Joshi, A.V.; Steppan, J.J.; Taylor, D.M.; Elangovan, S. Solid electrolyte materials, devices, and applications. *J. Electroceram.* **2004**, *13*, 619–625. [CrossRef]
10. Figueiredo, F.M.L.; Marques, F.M.B. Electrolytes for solid oxide fuel cells. *Wiley Interdiscip. Rev. Energy Environ.* **2013**, *2*, 52–72. [CrossRef]
11. Smith, L.; Ibn-Mohammed, T.; Yang, F.; Reaney, I.M.; Sinclair, D.C.; Koh, S.C.L. Comparative environmental profile assessments of commercial and novel material structures for solid oxide fuel cells. *Appl. Energy* **2019**, *235*, 1300–1313. [CrossRef]
12. Gu, S.; Xu, B.; Yan, Y. Electrochemical energy engineering: A new frontier of chemical engineering innovation. *Annu. Rev. Chem. Biomol. Eng.* **2014**, *5*, 429–454. [CrossRef]
13. Mahapatra, M.K.; Singh, P. Fuel Cells: Energy Conversion Technology. In *Future Energy*; Elsevier: Amsterdam, The Netherlands, 2014; pp. 511–547. [CrossRef]
14. Zhu, B. Solid oxide fuel cell (SOFC) technical challenges and solutions from nano-aspects. *Int. J. Energy Res.* **2009**, *33*, 1126–1137. [CrossRef]
15. Varga, Á. Introduction to Fuel Cell Technology. In *Fuel Cell Electronics Packaging*; Springer: Berlin/Heidelberg, Germany, 2007; pp. 1–32. [CrossRef]
16. Hussain, S.; Yangping, L. Review of solid oxide fuel cell materials: Cathode, anode, and electrolyte. *Energy Transit.* **2020**, *4*, 113–126. [CrossRef]
17. Wang, W.; Su, C.; Wu, Y.; Ran, R.; Shao, Z. Progress in solid oxide fuel cells with nickel-based anodes operating on methane and related fuels. *Chem. Rev.* **2013**, *113*, 8104–8151. [CrossRef]
18. Sun, C.; Hui, R.; Roller, J. Cathode materials for solid oxide fuel cells: A review. *J. Solid State Electrochem.* **2010**, *14*, 1125–1144. [CrossRef]
19. Le, M.-V.; Tsai, D.-S.; Nguyen, T.-A. BSCF/GDC as a refined cathode to the single-chamber solid oxide fuel cell based on a LAMOX electrolyte. *Ceram. Int.* **2018**, *44*, 1726–1730. [CrossRef]
20. Curi, M.; Silva, E.R.; Furtado, J.G.M.; Ferraz, H.C.; Secchi, A.R. Anodes for SOFC: Review of material selection, interface and electrochemical phenomena. *Quím. Nova* **2021**, *44*, 86–97. [CrossRef]
21. El Khal, H.; Cordier, A.; Batis, N.; Siebert, E.; Georges, S.; Steil, M.C. Effect of porosity on the electrical conductivity of LAMOX materials. *Solid State Ion.* **2017**, *304*, 75–84. [CrossRef]
22. Yokokawa, H.; Sakai, N.; Horita, T.; Yamaji, K.; Brito, M.E. Electrolytes for solid-oxide fuel cells. *MRS Bull.* **2005**, *30*, 591–595. [CrossRef]
23. Marrero-López, D.; Peña-Martínez, J.; Ruiz-Morales, J.C.; Pérez-Coll, D.; Martín-Sedeño, M.C.; Núñez, P. Applicability of $La_2Mo_{2-y}W_yO_9$ materials as solid electrolyte for SOFCs. *Solid State Ion.* **2007**, *178*, 1366–1378. [CrossRef]
24. Barelli, L.; Bidini, G.; Cinti, G.; Ottaviano, A. SOFC regulation at constant temperature: Experimental test and data regression study. *Energy Convers. Manag.* **2016**, *117*, 289–296. [CrossRef]
25. Huang, S.; Yang, C.; Chen, H.; Zhou, N.; Tucker, D. Coupling impacts of SOFC operating temperature and fuel utilization on system net efficiency in natural gas hybrid SOFC/GT system. *Case Stud. Therm. Eng.* **2022**, *31*, 101868. [CrossRef]
26. Zakaria, Z.; Abu Hassan, S.H.; Shaari, N.; Yahaya, A.Z.; Boon Kar, Y. A review on recent status and challenges of yttria stabilized zirconia modification to lowering the temperature of solid oxide fuel cells operation. *Int. J. Energy Res.* **2020**, *44*, 631–650. [CrossRef]
27. Jin, Z.; Yue, Y.; Xiong, H.; Chen, X.; Qiu, M.; Fan, Y. A novel low-temperature densification method for the construction of YSZ electrolyte membranes derived from nanoparticles. *J. Membr. Sci.* **2025**, *734*, 124373. [CrossRef]
28. Zha, S.; Moore, A.; Abernathy, H.; Liu, M. GDC-based low-temperature SOFCs powered by hydrocarbon fuels. *J. Electrochem. Soc.* **2004**, *151*, A1128–A1133. [CrossRef]
29. Slomski, H.S.; Rowberg, A.J.E.; Van Winkle, M.; Nagle-Cocco, L.A.V.; Strange, N.A.; Kane, N.; Hartvigsen, J.L.; Casteel, M.J.; Ginley, D.S.; Wood, B.C.; et al. The structure, composition, and performance impact of a YSZ-GDC interdiffusion layer in solid oxide electrolysis cells. *J. Power Sources* **2026**, *669*, 239398. [CrossRef]
30. Lee, J.I.; Ghosh, E.; Yu, H.; Kim, H.; Gopalan, S.; Basu, S.; Pal, U. Comparison of degradation between non-infiltrated and GDC-infiltrated fuel electrode in Solid Oxide Cells (SOCs) under long-term operation. *J. Power Sources* **2025**, *654*, 237793. [CrossRef]
31. Lacorre, P.; Goutenoire, F.; Bohnke, O.; Retoux, R.; Laligant, Y. Designing fast oxide-ion conductors based on $La_2Mo_2O_9$. *Nature* **2000**, *404*, 856–858. [CrossRef]
32. Goutenoire, F.; Isnard, O.; Retoux, R.; Lacorre, P. Crystal structure of $La_2Mo_2O_9$, a new fast oxide-ion conductor. *Chem. Mater.* **2000**, *12*, 2575–2580. [CrossRef]
33. Evans, I.R.; Howard, J.A.K.; Evans, J.S.O. The crystal structure of α-$La_2Mo_2O_9$ and the structural origin of the oxide ion migration pathway. *Chem. Mater.* **2005**, *17*, 4074–4077. [CrossRef]

34. Georges, S.; Goutenoire, F.; Altorfer, F.; Sheptyakov, D.; Fauth, F.; Suard, E.; Lacorre, P. Thermal, structural and transport properties of the fast oxide-ion conductors $La_{2-x}R_xMo_2O_9$ (R = Nd, Gd, Y). *Solid State Ion.* **2003**, *161*, 231–241. [CrossRef]
35. Ali, M.; Wani, B.; Bharadwaj, S. Phase transition in LAMOX type compounds. *J. Therm. Anal. Calorim.* **2009**, *96*, 463–468. [CrossRef]
36. Georges, S.; Goutenoire, F.; Bohnke, O.; Steil, M.C.; Skinner, S.J.; Wiemhoefer, H.D.; Lacorre, P. The LAMOX family of fast oxide-ion conductors: Overview and recent results. *J. New Mater. Electrochem. Syst.* **2004**, *7*, 51–58. [CrossRef]
37. Fang, Q.; Wang, X.; Cheng, Z.; Zhang, G. Research status of novel $La_2Mo_2O_9$-based oxide-ion conductors. *Front. Mater. Sci. China* **2007**, *1*, 7–15. [CrossRef]
38. Das, A.; Shajahan, I.; Dasari, H.P.; Saidutta, M.B.; Dasari, H. Dilatometer studies on LAMOX based electrolyte materials for solid oxide fuel cells. *Mater. Chem. Phys.* **2021**, *258*, 123958. [CrossRef]
39. Hchicha, K.; Mhadhbi, N.; Guesmi, A.; Soltani, T.; Hamadi, N.B.; Naïli, H. New Synthetic Route for Reaching Higher Phase Stabilization in LAMOX-Based Electrolyte for Solid Oxide Fuel Cells. *Eur. J. Inorg. Chem.* **2023**, *26*, e202200696. [CrossRef]
40. Siddharth; Sil, A.; Bysakh, S. Effect of K doping on Mo^{6+} stability and ionic conductivity study in $La_2Mo_2O_9$ as oxide-ion conductor. *Mater. Res. Express* **2019**, *6*, 056203. [CrossRef]
41. Shiwankar, S.S.; Acharya, S.A.; Mendhe, A.B.; Shirbhate, S.M.; Singh, M.; Sagdeo, A. Structural complexity and ionic conductivity in gadolinium and tungsten co-doped $La_2Mo_2O_9$: A potential electrolyte for IT-SOFCs. *Electrochim. Acta* **2025**, *524*, 145944. [CrossRef]
42. Malavasi, L.; Kim, H.; Billinge, S.J.L.; Proffen, T.; Tealdi, C.; Flor, G. Nature of the monoclinic to cubic phase transition in the fast oxygen ion conductor $La_2Mo_2O_9$ (LAMOX). *J. Am. Chem. Soc.* **2007**, *129*, 6903–6907. [CrossRef] [PubMed]
43. Mhadhbi, N.; Jabeur, W.; Guesmi, A.; Houas, A.; Hamadi, N.B.; Naïli, H. Phosphorus-substitution effect on the phase stabilization, electrical and spectroscopic properties of LAMOX-based electrolyte for solid oxide fuel cells. *RSC Adv.* **2023**, *13*, 30168–30175. [CrossRef]
44. Kiefer, M.A.; Porter, E.A.; Billing, C.; Stone, K.H.; Billing, D. Accelerated Solid-State Synthesis of LAMOX via Mechanical Activation. *SSRN* **2025**, 5600064. [CrossRef]
45. Tealdi, C.; Chiodelli, G.; Flor, G.; Leonardi, S. Electrode stability and electrochemical performance of Lamox electrolytes under fuel cell conditions. *Solid State Ion.* **2010**, *181*, 1456–1461. [CrossRef]
46. Weber, I.T.; Baracho, P.R.; Rangel, F.; Paris, E.C.; Muccillo, E.N.S. Pure and Gd doped LAMOX powders and thin films obtained by chemical route. *Mater. Sci. Technol.* **2009**, *25*, 1346–1350. [CrossRef]
47. Kadam, G.A.; Patil, S.A.; Patil, B.B.; Kumbhar, S.S.; Kumbhar, S.S.; Madake, S.B.; Kadam, L.D.; Ma, Y.R.; Kadam, S.A.; Nimat, R.K. Dielectric behavior and phase transition of $La_2Mo_2O_9$ films synthesized by spray pyrolysis technique. *J. Mater. Sci. Mater. Electron.* **2023**, *34*, 387. [CrossRef]
48. Žalga, A.; Gaidamavičienė, G.; Gricius, Ž.; Užpurvytė, E.; Gadeikis, J.; Diktanaitė, A.; Barré, M.; Šalkus, T.; Kežionis, A.; Kazakevičius, E. Aqueous sol–gel synthesis, thermoanalytical study and electrical properties of $La_2Mo_2O_9$. *J. Therm. Anal. Calorim.* **2018**, *132*, 1499–1511. [CrossRef]
49. Kakihana, M.; Kobayashi, M.; Tomita, K.; Petrykin, V. Application of water-soluble titanium complexes as precursors for synthesis of titanium-containing oxides via aqueous solution processes. *Bull. Chem. Soc. Jpn.* **2010**, *83*, 1285–1308. [CrossRef]
50. Jeitschko, W. Crystal structure of $La_2(MoO_4)_3$, a new ordered defect scheelite type. *Struct. Sci.* **1973**, *29*, 2074–2081. [CrossRef]
51. Xue, J.S.; Antonio, M.R.; Soderholm, L. Polymorphs of Ln_2MoO_6: A neutron diffraction investigation of the crystal structures of La_2MoO_6 and Tb_2MoO_6. *Chem. Mater.* **1995**, *7*, 333–340. [CrossRef]
52. Žalga, A.; Gaidamavičienė, G.; Elsts, E.; Gabrusenoks, J.; Popov, A.I. The effect of lanthanum content on the composition and phase transition characteristics of the multicomponent $La_{2\pm x}Mo_2O_{9\pm 3/2x}$ system. *J. Therm. Anal. Calorim.* **2025**, *150*, 6001–6011. [CrossRef]
53. Nakamoto, K. *Infrared and Raman Spectra of Inorganic and Coordination Compounds: Theory and Applications in Inorganic Chemistry*; John Wiley & Sons: Hoboken, NJ, USA, 2008; 426p.
54. Dammak, K.; Mhadhbi, N.; Tozri, A.; Naïli, H. Influence of Isovalent Partial Sulfur Substitution on the Structural, Thermal, Electrical and Spectroscopic Properties of $La_2Mo_2O_9$ Oxide Ion Conductors. *Eur. J. Inorg. Chem.* **2022**, *2022*, e202200165. [CrossRef]
55. Kakinuma, K.; Takahashi, N.; Yamamura, H.; Nomura, K.; Atake, T. Electrical conductivity and local distortion of $(Ba_{0.5}La_{0.5})_2In_2O_{5.5}$ doped with divalent or tetravalent cation in in-site. *Solid State Ion.* **2004**, *168*, 69–74. [CrossRef]
56. Patel, A.; Singh, S.; Nath, C. Investigation of ion transport properties in Er–W co-doped $La_2Mo_2O_9$ electrolytes. *Phys. B Condens. Matter* **2023**, *661*, 414955. [CrossRef]